Bubble Dynamics in Ultrasound

Cheryn Pisciotta Engebrecht

A thesis submitted in partial fulfillment of
the requirements for the degree of

Master of Science in Mechanical Engineering

University of Washington

2009

Program Authorized to Offer Degree:
Mechanical Engineering

University of Washington
Graduate School

This is to certify that I have examined this copy of a master's thesis by

Cheryn Pisciotta Engebrecht

and have found that it is complete and satisfactory in all respects,
and that any and all revisions required by the final
examining committee have been made.

Committee Members:

_____
Alberto Aliseda

_____
Pascale Lelong

_____
James Riley

Date: _____

Signature_____

Date_____

TABLE OF CONTENTS

LIST OF FIGURES

LIST OF TABLES

ACKNOWLEDGMENTS

First and foremost, I truely appreciate the guidance and "open door" policy of my advising professor Dr. Alberto Aliseda. His dedication to my project provided an efficient work environment which I thrived in. I wholeheartedly acknowledge the National Science Foundation for their faith in the project and financial support that this project required to exist. To my labmates: Thank you for helping me through any frustrating pitfalls by keeping my spirits up with your laughter. I would also like to dedicate this thesis to my grandfather, Dr. Richard Engebrecht, whose life long devotion to education has helped me recognize the intangible gifts of knowledge that all of my family and friends have given me.

Chapter 1

INTRODUCTION

Ultrasound has been used for many years to view the interior of the human body. More recently, the distinguishable impedance properties of microbubbles have been used in the medical field as an ultrasound contrast agent (UCA) which allows doctors to easily differentiate the pulsing blood from any surrounding tissue. Recently, doctors have observed many bubble dynamics properties without being able to explain them mathematically.

The motivation for this research extends from many different backgrounds and disciplines. A combination of physics research and medical research brings us to the questions we ask today. How do we manipulate microbubbles? Once we know this, how do we predict where they are going? And finally, what kinds of applications will allow us to use this knowledge to our advantage? This thesis aims to combine the knowledge on bubble dynamics from fluid mechanics with acoustics and biological observations made by doctors, and provide a basis for a methodical technique for microbubble manipulation.

This introduction will first discuss the background information related to ultrasound and how its uses fit into the medical field. Following that, a review of the relationship between ultrasound and microbubbles and how specific types of microbubbles are used within the field of medicine. The introduction will then be given on the primary contributors responsible for the fluids behind the dynamics of the microbubbles in a liquid when they are under the influence of an ultrasound transducer. This is followed up by a quick discussion on the material that has branched out from the original papers related to microbubbles in ultrasound. Finally, the specific goals of this thesis are stated as a transition into the rest of the paper.

1.1 Ultrasound in Medicine

In medical imaging, ultrasound waves (defined by frequencies above the audible range $\geq$20,000 Hz) travel through the body and create images based on the difference in impedance between tissues. The reflected signal is captured by the same transducer that emits the signal and a computer program translates the reflected sound waves into a black and white image. Many people are familiar with this technique because of the images taken during a woman's pregnancy. These images are a great example of how difficult it is to distinguish between the different materials present in the human body.

The characteristic impedance (Z) of a material is equal to the density of the medium times the speed of sound through the it (ρc). In general, a large difference in impedances between two mediums will create clear definition in an ultrasonic image. Unfortunately, human muscle, fat, artery walls, and blood all have very similar impedances (about 1.7 MRayls = $1.7 \frac{MPa \cdot s}{m}$) and produce images with little contrast. Air however, has a very low impedance (about 400 Rayls at room temperature) compared to human tissue and can be injected into arteries in the form of microbubbles to provide contrast. When millions of microbubbles are released into the blood stream, the contrast between the flowing blood and the surrounding tissue in an ultrasonic image becomes much clearer, thus the name Ultrasound Contrast Agents (UCAs).

1.2 Ultrasound Contrast Agents (Microbubbles)

Some of the first contrast agents were made using polymer coated microbubbles [31]. In the early 1990's common brands like Albunex and Levovist were introduced [12, 15]. As time goes on, UCAs become more easily injected, more robust and safer to have in a human's blood stream.

UCAs have been used as a diagnostic technique since the mid 1980's [7]. In 1986 they were used during shunt surgery to locate the catheter and determine the flow pattern of the blood or fluid in the brain [32]. Since then, they have been used to diagnose vesicoureteral reflux (VUR) in children and young adults under the age of 20 [5]. This

study was not only successful in diagnosing if the young adults had VUR, but also helpful in confirming if they did not have VUR. Another study uses a specific formula for contrast agents to confirm if a patient has tubal patency (a blockage in fallopian tubes) [9]. This information is useful for determining which fertility drug to treat the woman with. Other diseases that can be diagnosed using UCAs include the detection of focal hepatic lesions in the liver [30], coronary stenosis, carotid artery stenosis/ occlusion [14] and the evaluation of relative changes in myocardial perfusion [10].

Sometimes, during the diagnostic tests, the microbubbles would collapse in on themselves (inertial cavitation). This would lead to the rupture of some of the endothelial cells on the interior walls of the artery which eventually caused further complications for the patient. Later, scientists tried using these collapsing bubbles to help cure or reduce the symptoms of certain diseases.

One area in which doctors are studying the use of bubble cavitation as a positive solution is in thrombolysis [6]. In combination with an injected tissue plasminogen activator (tPA), ultrasound contrast agents are placed near an arterial blood clot and pulsed until they collapse. This produces enough force to break down the blood clot so that tPA can penetrate the clot and leave its fibrin structure. Figure 1.1 shows the blood flow in a bifurcation with one arm under complete occlusion. This demonstrates how little blood flow there is in such regions and how slow it would be to rely on diffusion alone to help the drug travel to this area.

Eventually, drugs such as tPA will be used to coat the microbubbles and they will be the *only* tool needed to break up blood clots. The future goals of this research include determining the dynamics of microbubbles used in arteries and how to use ultrasound to control them. With the findings of this research, scientists and doctors should eventually be able to efficiently and repeatably direct drug coated microbubbles to low-flow or no-flow regions in diseased arteries.

UCAs designed for the medical industry differ from regular air bubbles both in their size and their surface tension properties caused by the lipid layer. This layer prevents the bubbles from coalescing and creating a potentially dangerous larger air bubble.

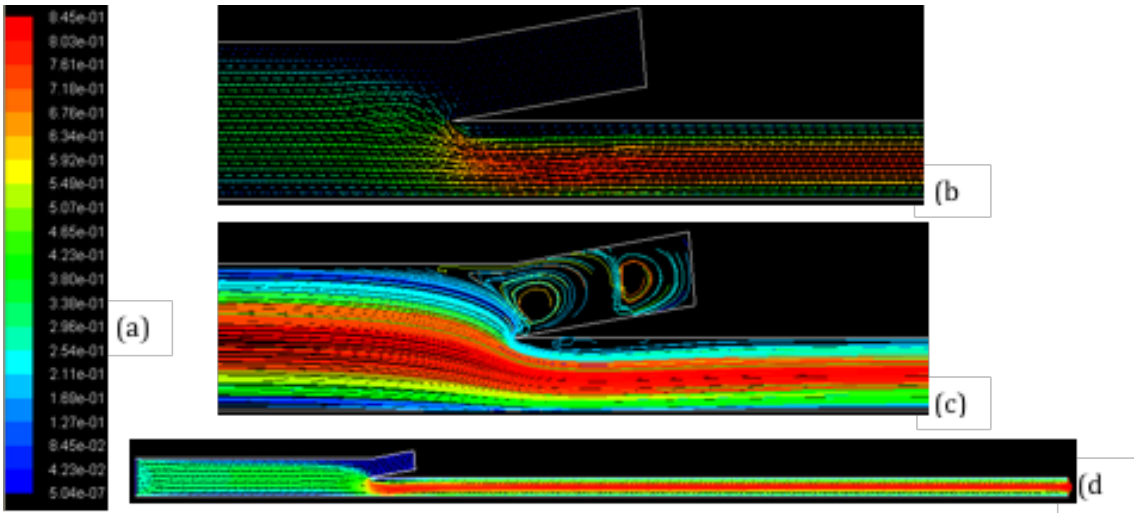

Figure 1.1:]

Top arm of bifurcation is completely blocked by blood clot. There is little to no flow in the entire arm even though the blockage is a few centimeters up. Diffusion is the only current mechanism capable of taking a drug from the blood stream to the site of the blockage. (a) Color velocity scale for (b) and (d). Magnitudes in m/s. (b) Velocity vectors show velocity in both length and color. (c) Although the pathlines here show two recirculation regions near blockage, the velocities in this area are so small, the recirculation is practically negligible. Note: The colors here simply denote the difference between each particle and do not correlate with the scale used for the rest of the images. (d) Full view of flow up and down stream

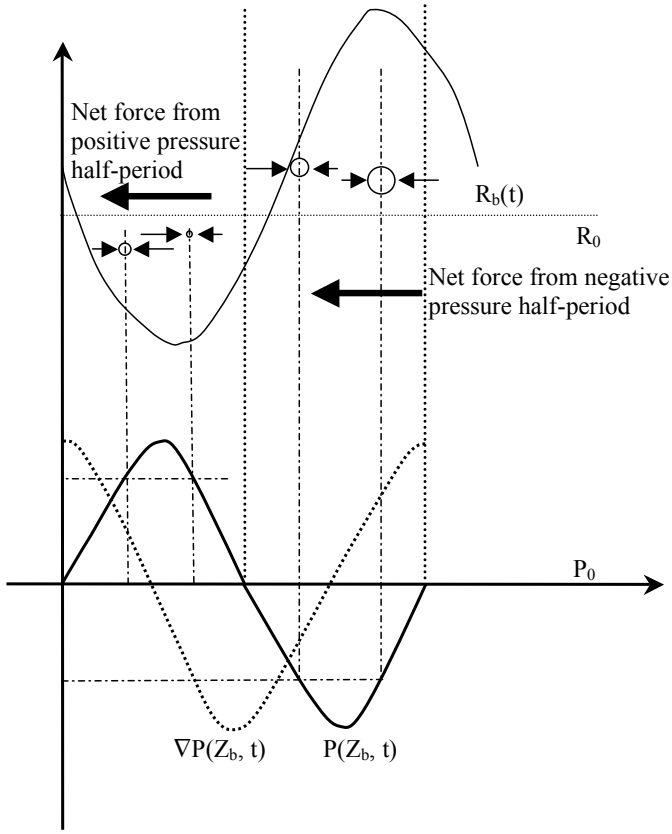

Figure 1.2: R_b, R_o, ∇P, P, and P_o are the bubble radius as a function of time, the equilibrium bubble radius, the spatial derivative of pressure as a function of distance from the transducer and time, pressure as a function of distance from the transducer and time, and average pressure respectively. The relationship between spatial derivative of the pressure and the bubble volume causes a net force in the direction of the traveling pressure wave.

1.3 Bubble Dynamics in Ultrasound

The following section describes the previous contributions made in the area of bubble dynamics in ultrasound.

1.3.1 Bjerknes Force

In the late 1800's, Vilhelm Bjerknes was introduced to the study of hydrodynamics by his father and respected mathematician, Carl Bjerknes. Soon Vilhelm's interests moved toward geophysics and he became interested in weather pattern analyses where his work eventually helped predict weather all over the world. His contributions to the current research stem from his lecture given in 1906 called *Fields of Force* [1] which touched on the interactions of fluids with different densities.

Bjerknes is now credited for the equation which describes the force on a low density medium created by a pressure wave that travels through a high density medium. In the current research, the low density medium is an air bubble and the high density medium is water. The "Bjerknes force" describes a force acting in the direction of a traveling pressure wave on an air bubble. This force is created by a phase lag between the pulsing bubble volume (created by the pressure wave of the ultrasound) and the pressure wave itself [8, 4]. A graphical image of this phase lag and the reaction of the bubble can be seen figure 1.2.

An air bubble that exists, undisturbed and un-forced in a water tank experiences a force balance between the volume of air inside the bubble, the hydrostatic pressure, and the surface tension between the gas and the liquid. When a bubble is subjected to a pressure wave created by ultrasound, inertial and ultrasound pressure wave forces are introduced and the original forces become unbalanced by the introduction of these perturbances.

When the low pressure section of the pressure wave hits the surface of the bubble, it begins to expand due to the now lower pressure in the water just outside the walls of the bubble. As the bubble expands, it's walls push the water away from the center of the bubble. This moving mass of fluid adds a strong inertia to the dynamics of the bubble

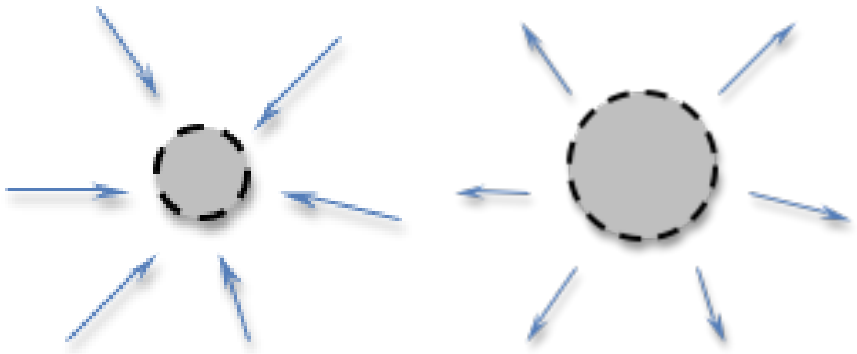

(a) Inward inertia (b) Outward Inertia

Figure 1.3: Inertial effects (blue arrows) of liquid on gas bubble

due to the large density ratio between the liquid and the gas inside the bubble. As the pressure reaches its minimum value for a given oscillation, the inertial forces from the water around the bubble are still expanding the bubble outward (Figure 1.3(b)). As the peak of the pressure wave passes the bubble, the volume does not immediately begin to decrease because the liquid inertia around the bubble is still trying to expand it. This creates a delay (or phase lag) between the pressure fluctuations and the bubble's volume oscillations. The same is true with different magnitudes for the contraction phase (Figure 1.3(a)).

As seen in figure 1.2, the size of the bubble closely corresponds with the inverse of the ultrasonic pressure field created by a transducer. In other words, the bubble is its largest just after the pressure wave has reached its minimum and smallest just after the pressure wave has reached its maximum.

1.3.2 Computational Models

There have been many computational simulations of bubble dynamics, all of them taking into consideration various predicted factors that might effect the dynamics of bubbles under certain conditions. These potential factors include the non-equilibrium phase change

of the bubble wall [11], thermal diffusion [24, 13], and viscous effects of the liquid [28]. In 2005, a group from the University of Tokyo used computational analysis to observe that microbubble clusters act differently than a single microbubble when under the influence of resonant frequency ultrasound [21]. When including the effects of the evaporation and condensation of the liquid and the heat transfer at the bubble wall, as well as the compressibility of the fluid, they found that the bubble at the center of the cluster actually generates higher pressure than if it was just in isolation. The large cluster also induces larger cavitation effects than the combined effect of each individual bubble cavitation. This is interesting and important for scientists to remember when considering UCAs in blood vessels in that they should be diluted before injecting them into the blood stream.

1.3.3 Previous Experimental Work

Many scientists have looked at the oscillations of bubbles in a stationary environment [2, 29], however, most of these tests are conducted in confined spaces which provides little information for the challenges which arise in the current experimental work. The only studies conducted that consider the dynamics of microbubbles in an ultrasonic field in a large tank (such as the current project) have been related to sonoluminescence [22]. Using the Bjerknes force described earlier, the ultrasound is used to make microbubbles oscillate nonlinearly. The bubbles generally contract faster than they expand. Over time, this produces a larger and larger average bubble radius size due to rectified diffusion. At a certain point, the large bubble collapses adiabatically in a very short amount of time, leaving the interior of the bubble to have temperatures up to 5000 K. This burst of energy creates a 'spark' that emits light, therefore named sonolumninescence. Generally, sonoluminescence is observed at the antinode of a standing sound pressure wave. This phenomenon changes slightly if there is more than one bubble under the influence of the ultrasound because of the re-radiation (secondary Bjerknes force) that comes off of each bubble.

The challenges that have not been addressed in previous experiments that will be addressed here are the large ratio between the bubble size and its container (making it

hard to visualize bubbles in this unconfined environment), and the large focal distance necessary to obtain these images (where usually a microscope with a focal range of 1 mm is used to image such small objects).

1.4 Microbubble formation/creation techniques

Over the years, the way in which microbubbles have been created for use in experiments has changed along with the research that involves them. Laser impulses have been used to form microbubbles since the 1970's [17, 2, 29]. Here, a strong pulse hits a liquid surface and creates a cavity which forms a microbubble filled with liquid vapor and dissolved gasses. Although this technique was invented many years ago, it is still used in the present day [34]. Chemical compounds used in a lipid layer, form the more robust microbubbles usually called Ultrasound Contrast Agents. Also recently, a group of chemists in Canada have discovered a new technique for making a single microbubble at at time using a micropipette [23]. In the current research, both water bubbles and UCAs are used for their strengths in different areas.

1.5 Objectives of this Thesis

The objectives of this research are:

- To design an experiment which demonstrates that bubbles under the influence of a given ultrasound field (characterized by its frequency and intensity), will be forced to rise slower than those microbubbles not in an ultrasonic field.

- To compare data from the current experimental configuration to theoretical predictions based on Bjerknes force

- To characterize the effect of the ultrasound field on microbubbles that are subjected to a unidirectional flow field that is perpendicular to the pressure waves emitted by the ultrasound transducer

Chapter 2 introduces the theoretical equations that model bubble dynamics. Chapter 3 describes experimental setup that leads to the data displayed and analyzed in chapter 4. The results from these experiments are compared to previously found data and figures and presented in chapter 5. Chapter 6 summarizes all the conclusions that can be obtained from this research. A description of future work proposed to continue this study is presented in chapter 7.

Chapter 2

BUBBLE DYNAMICS

2.1 Freely Oscillating Bubble

Supposing an oscillating bubble under water is constantly spherical and that no energy is dissipated by heat or phase changes, it can be compared to a spring and mass system in simple harmonic motion. This zeroth order approximation assumes that the elastic quality of the air inside the bubble and the inertia of the water are the spring and mass respectively, one may excite the system by pulling the bubble outward in all directions and letting go. The oscillating system will have a resonant frequency associated with it which depends on the equilibrium radius of the bubble. Equation 2.1 shows how the resonant frequency of a bubble relates to its radius.

$$F_R = \frac{1}{2\pi}\frac{1}{R_o}\sqrt{\frac{3\gamma p_{air}}{\rho_{water}}} \tag{2.1}$$

F_R is the resonant frequency, R_o is the equilibrium radius, ρ_{water} is the density of water and γ is the specific heat ratio [20] (1.4 for air).

This may be the frequency that a freely oscillating bubble resonates at, however, it is also a good approximation for the frequency of a pressure wave that will oscillate a given size bubble diameter. In the simplist case, for an air bubble (air at 1 atm) in water, equation 2.1 simplifies to $F_R R_o = 3m/s$.

2.2 Forced Bubble

When a bubble, surrounded by liquid, is subjected to the oscillating pressure waves of an acoustic field, it reacts by undergoing a volume oscillation that corresponds with the pressure oscillations (see figure 1.2). However, due to viscous, thermal and pressure radiation losses experienced at the barrier between the gas and liquid, the acoustic pressure

wave oscillations and the bubble volume oscillations become out of phase and the bubble experiences a translational force. The following section derives the theoretical equations that describe this motion.

2.2.1 Rayleigh-Plesset Equation

A spherical bubble under the influence of a pressure wave will experience a change in volume, and therefore, a change in radius, which in turn, changes the force from the pressure wave (Force=Pressure x Area). The following steps describe the derivation for the Rayleigh-Plesset equation which characterizes the radius of an oscillating bubble in a time varying pressure field.

Assuming that R_o is the equilibrium bubble radius and P_o is the equilibrium pressure inside the bubble, then $R = R_o$ and $P_{total} = P_o$ at time t=0. At times larger than t=0, $P_{total} = P(z,t) + P_o$ where $P(z,t)$ is the pressure induced by the ultrasound transducer.

The kinetic energy of the liquid surrounding the bubble comes from its inertial forces and can be described as [18]:

$$\frac{1}{2}\rho \int_R^\infty \dot{r}^2 4\pi r^2 \, dr \tag{2.2}$$

where r is the radial coordinate of the water if the origin is at the center of the bubble under investigation.

If the liquid surrounding the bubble is incompressible, then as the volume of the bubble increases, the volume of the liquid around the bubble will have to increase the same amount, and at the same rate. So, if R(t) is the bubble radius at a given time, the volume of the bubble will be $\frac{4}{3}\pi R(t)^3$. If a control volume is taken around the bubble so that it is a distance, r, from the center of the bubble, its volume is $\frac{4}{3}\pi r(t)^3$. The rate of the volume change (dV/dt) for the bubble is $4\pi R^2 \dot{R}$ and due to incompressibility is $4\pi r^2 \dot{r}$ for the liquid surrounding the bubble. Equating these two expressions for dV/dt and slightly rearranging terms gives another expression:

$$\frac{dr/dt}{dR/dt} = \frac{R^2}{r^2} \tag{2.3}$$

Substituting equation 2.3 into equation 2.2 and integrating to get the work done by the bubble on the liquid you obtain $2\pi\rho R^3(dR/dt)^2$. The following equation equates the work done by the fluid with the work done on the fluid:

$$\int_{R_o}^{R} (P_L - P_\infty)\, 4\pi r^2\, dr = 2\pi R^3 \dot{R}^2 \rho \tag{2.4}$$

where P_L is the pressure just outside the bubble walls and P_∞ is the hydrostatic pressure far away from the bubble.

Additionally, with a surface tension σ, the internal pressure of a bubble residing in that liquid is $P_o + (2\sigma/R_o)$ and the pressure of the gas phase in the bubble is $P_o + (2\sigma/R_o) - P_v$ where P_v is the the vapor pressure. Assuming the addition of an acoustic pressure wave, $P(z,t)$, the radius will undergo polytropic expansion. The pressure of the gas inside the bubble is:

$$\left(P_o + \frac{2\sigma}{R_o} - P_v\right)\left(\frac{R_o}{R}\right)^{3\gamma} \tag{2.5}$$

where γ is the polytropic constant for the gas evolution (from 1 for isothermal processes to 1.4 for adiabatic processes). The hydrostatic pressure just outside the bubble walls would be:

$$P_L = \left(P_o + \frac{2\sigma}{R_o} - P_v\right)\left(\frac{R_o}{R}\right)^{3\gamma} - \frac{2\sigma}{R} \tag{2.6}$$

where the term$\frac{2\sigma}{R}$ is the pressure caused by the surface tension of the bubble pushing outward at a given R.

However, a third term was added to the equation in 1952 [26] by Poritsky that includes the effects of the viscosity of the liquid which is necessary to ensure continuity of normal stresses at the wall of the bubble. The final equation for the hydrostatic pressure just outside the bubble wall is:

$$P_L = \left(P_o + \frac{2\sigma}{R_o} - P_v\right)\left(\frac{R_o}{R}\right)^{3\gamma} - \frac{2\sigma}{R} - \frac{4\mu\dot{R}}{R} \tag{2.7}$$

where μ is the dynamics viscosity of the liquid [19]. The Rayleigh-Plesset equation, equation 2.8, is found by substituting equation 2.7 into equation 2.4. As is, this equation can only be solved through iteration techniques.

$$\rho\left(R\ddot{R} + \frac{3\dot{R}^2}{2}\right) = \left(P_o + \frac{2\sigma}{R_o} - P_v\right)\left(\frac{R_o}{R}\right)^{3\gamma} - \frac{2\sigma}{R} - \frac{4\mu\dot{R}}{R} - P_\infty - P(z,t) \tag{2.8}$$

2.2.2 Bjerknes Force Equations

In order to gain insight on the resonance behavior of bubbles, certain limitations are put on equation 2.8 so that it may be approximated analytically. Assume the acoustic pressure wave is made of small amplitude oscillations such as:

$$P(z,t) = P_A cos(\omega t - kz) \tag{2.9}$$

where P_A is the amplitude of the ultrasound pressure wave, $\omega = 2\pi f$ is the angular frequency, $k = \frac{\omega}{c}$ is the wavenumber and c is the speed of sound in the liquid. The gradient of the pressure is then:

$$\nabla P(z,t) = kP_A sin(\omega t - kz) \tag{2.10}$$

If the radius oscillations of the bubble correspond to the peaks and valleys of the pressure wave, and the radius oscillations are small in comparison to the equilibrium radius, then the equation for the bubble radius as a whole can be expressed as:

$$R = R_o + R_\varepsilon(t) = R_o - R_{\varepsilon o} e^{i\omega_o t} \tag{2.11}$$

where R is the bubble radius, $R_\varepsilon = -R_{\varepsilon o} e^{i\omega_o t}$ represents the small amplitude oscillations that the bubble wall follows about the mean radius R_o, $\omega_o = 2\pi F_R$ is the resonant angular frequency, and the negative sign corresponds to the decreasing size of the bubble due to the inward pressure force from the water around it.

If $R_\varepsilon << R_o$, and vapor pressure and viscosity are negligible, the simplified solution of equation 2.8 gives the volume as a function of time:

$$V(t) = V_o \left(1 - \left(\frac{3R_{max}}{R_o}\right) cos(wt - kz - \theta)\right) \tag{2.12}$$

where $V_o = \frac{4}{3}\pi R_o^3$ is the equilibrium bubble volume, R_{max} is the maximum bubble radius, and θ is the phase lag between the acoustic pressure wave and the volume oscillations. R_{max} is described by the equation below:

$$R_{max} = \frac{P_A}{R_o \rho \omega^2 \sqrt{\left((\frac{\omega_o}{\omega})^2 - 1\right)^2 + \left(\frac{2\beta_{tot}}{\omega}\right)^2}} \tag{2.13}$$

where $\omega_o = 2\pi f_o$ is the resonant frequency for a bubble with the equilibrium radius of R_o and β_{tot} is the dissipative constant that takes into consideration all of the factors that effect the bubble damping (such as viscous and thermal losses) [18]. The θ in equation 2.12 corresponds to the phase lag which is related to the dissipative constant and angular frequencies present.

$$\theta = sin^{-1}\left(\frac{2\beta_{tot}\omega}{\sqrt{(\omega_o^2 - \omega^2)^2 + (2\beta_{tot}\omega)^2}}\right) \tag{2.14}$$

A bubble with volume V that lies in a pressure gradient ∇P will experience a downward force that is equal to $V\nabla P$. In this case, the pressure oscillates in time and therefore the force is a function of time as well. The average net force however, is the time average of the total forces:

$$\langle F_{Bjrk}\rangle = \langle V(t)\nabla P(z,t)\rangle \tag{2.15}$$

where z is the distance between the transducer source and the bubble. Substituting equations 2.10 and 2.12 into equation 2.15 gives:

$$\begin{aligned}\langle F_{Bjrk}\rangle &= \langle V_o k P_A\left(1 - \left(\frac{3R_{max}}{R_o}\right)cos(wt - kz - \theta)\right)(sin(kz - \omega t))\rangle \\ &= V_o k P_A\left(\langle sin(kz - \omega t)\rangle\right) \\ &\quad -V_o k P_A\left(\frac{3R_{max}}{R_o}(\langle(sin^2(\omega t - kz)sin(\theta)\rangle + \langle cos(\omega t - kz)sin(\omega t - kz)\rangle cos(\theta)\right)\end{aligned} \tag{2.16}$$

In this case, the average of both the $\langle sin(kz-\omega t)\rangle$ and $\langle cos(\omega t-kz)sin(\omega t-kz)\rangle cos(\theta)$ terms go to zero. The $\langle(sin^2(\omega t - kz)\rangle$ goes to 1/2 and the force is simplified to be:

$$\langle F_{Bjrk}\rangle = V_o k P_A \frac{3R_{max}}{2R_o} sin(\theta) \tag{2.17}$$

Substituting equations 2.13 and 2.14 into equation 2.17 and simplifying, we obtain the average Bjerknes force.

$$\langle F_{Bjrk}\rangle = \frac{3V_o k P_A^2\left(\frac{2\beta_{tot}}{\omega}\right)}{R_o^2\rho\omega^2\sqrt{\left[\left(\left(\frac{\omega_o}{\omega}\right)^2 - 1\right)^2 + \left(\frac{2\beta_{tot}}{\omega}\right)^2\right]}} \tag{2.18}$$

2.3 Theoretical Bubble Rise Velocity

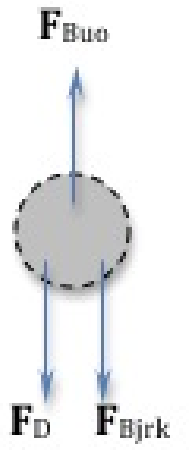

Figure 2.1: Free Body Diagram of forces on bubble in liquid and under the influence of an ultrasonic pressure wave. F_{Bjrk} is the Bjerknes (acoustic) force, F_D is the drag force and F_{Buo} is the buoyancy force.

Theoretically, the rise velocity of the bubble can be determined by balancing the forces on the bubble. Figure 2.1 shows the Bjerknes (acoustic) and drag forces pushing downward on the bubble, while the buoyant forces are pushing upward so that

$$F_{Bjrk} + F_D + F_{Buo} = 0 \tag{2.19}$$

The Bjerknes force, F_{Bjrk}, is represented by equation 2.18. The drag force, F_D is calculated based on the assumption that the bubble is freely rising with uniform motion. Therefore, the drag force is

$$F_D = \frac{1}{2}\rho \mathbf{v}^2 C_D(\pi R_o^2) \tag{2.20}$$

where πR_o^2 is the projected frontal area of a sphere. According to Crum and Eller [3], the upper limit of the drag coefficient is given by

$$C_D = \frac{24\chi}{R_e} \tag{2.21}$$

where R_e is the Reynolds number of the bubble and χ is a variable described below [16].

$$R_e = \frac{\rho \mathbf{v} D}{\mu} \tag{2.22}$$

$$\chi = 1 + 0.197 R_e^{0.63} + 2.6 \times 10^{-4} R_e^{1.38} \tag{2.23}$$

ρ is the density of the liquid, $\mathbf{v}$ is the total velocity of the bubble, D is the diameter of the bubble and μ is the dynamic viscosity of the liquid. Substituting equation 2.21 into equation 2.20 and simplifying, gives the overall equation for the drag force in terms of χ is:

$$F_D = 6\mathbf{v}\mu\pi R_o \chi \tag{2.24}$$

The buoyancy force, F_{Buo}, is defined by the density of the fluid (ρ) multiplied by the volume of the displaced fluid ($(4/3)\pi R_o^3$) and by the acceleration due to gravity ($\mathbf{g}$). After substituting the equation 2.18 and equation 2.24 into equation 2.19, one may solve for the theoretical rise velocity of the bubble.

$$\mathbf{v} = \frac{2\rho R_o^2 \mathbf{g} - F_{Bj} \frac{3}{2\pi R_o}}{9\mu\chi} \tag{2.25}$$

The theoretical rise velocity of a bubble may also be calculated without the influence of the Bjerknes force assuming that $F_{Bou} = F_D$ and solving for the rise velocity:

$$\mathbf{v} = \frac{2\rho R_o^2 \mathbf{g}}{6\mu\chi} \tag{2.26}$$

In both equations 2.25 and 2.26, it is important to realize that the velocity is present in both the left and right hand side of the equation (appears in χ term within the Reynolds number variable). Therefore, when calculating the rise velocity, an iteration technique must be used. The matlab code which runs this iteration can be found in Appendix C.

2.4 Saffman Lift

In the second set of experiments, the bubbles are inside a tube which carries water and bubbles perpendicular to the axis of the transducer. The addition of the constraint of the tube adds a shear element to the flow. Shear forces exist when fluid travels between two

plates so that the largest shear (proportional to du/dr where u(r) is the velocity profile in the tube and r is the radial distance from the center of the tube) occurs near the walls. This phenomena was first described analytically by Saffman [27] who assumed that the force originated from inertia effects and that the sphere was undergoing steady motion.

Assuming that a solid sphere (or bubble in this case) exists within shear flow and is spinning due to the variable velocity profile, a specific shear Reynolds number can be defined:

$$Re_{\dot{\gamma}} = \frac{\dot{\gamma} d^2}{\nu} \tag{2.27}$$

where $\dot{\gamma}$ is the shear rate, d is the diameter of the bubble, and ν is the kinematic viscosity of the liquid. If the Poiseuille velocity profile inside a tube of radius b is:

$$u = 2u_m(1 - \rho^2/b^2) \tag{2.28}$$

where u_m is the mean velocity, and ρ is the distance from the center axis, then the tube Reynolds number is $Re_{tube} = 2u_m b/\nu$.

A particle (or bubble) with radius, a, that is centered at ρ distance from the center axis, experiences a shear of magnitude $4u_m\rho/b^2$. If this bubble is slower than the local velocity of the liquid inside the tube, then it has a relative velocity V, and it has a viscosity reduced force of

$$F_{saff} = 324Va^2(\frac{u_m\rho}{\nu b^2})^{1/2} \tag{2.29}$$

towards the axis. Later, Poe and Acrivos [25] determined that this force was only valid if $Re_G < 0.1$. This force corresponds to an equivalent velocity towards the center of the tube defined by:

$$\frac{162V}{3\pi}\left(\frac{u_m\rho a^2}{\nu b^2}\right)^{1/2} \tag{2.30}$$

However, if the bubble travels faster than the fluid, the inertial effects and the Saffman force will impose a force away from the center axis of the tube.

Chapter 3

EXPERIMENTAL SETUP

This chapter gives a detailed description of the experimental setup used to collect the data shown in chapter 4. There are two sets of experiments conducted in this research. The first set of experiments measures the velocity of bubbles rising in a large open tank both with and without the influence of a transducer. This process will not discover any new correlations or theories, however, it will verify the experimental setup for the second set of experiments. The details of how the experiments are carried out are used in the second set of experiments which determine the effect of the Bjerknes force when it is applied to bubbles traveling in a phantom artery perpendicular to the axis of the transducer.

The first section of this chapter introduces the components that are present in the open tank experiments which simply measure the rise velocity of the bubbles with and without a transducer. The second section describes the components necessary in taking data that pertains to bubbles flowing perpendicular to the Bjerknes force.

3.1 Open Tank Rising Bubble Experiments

Figure 3.1 shows an overall view of what is involved in taking data for this experiment. Bubbles are created by a combination of forced air from the syringe pump and forced water from the heart simulation pump. The same flow that creates the bubbles, then injects the bubbles into the tank where they are left free to rise in front of the high speed camera (bubbles are backlit by lamp). The image is stored and the bubble velocity is obtained through image analysis. The rest of section will give a detailed description of the role that each major component plays in the open tank rising bubble experiment.

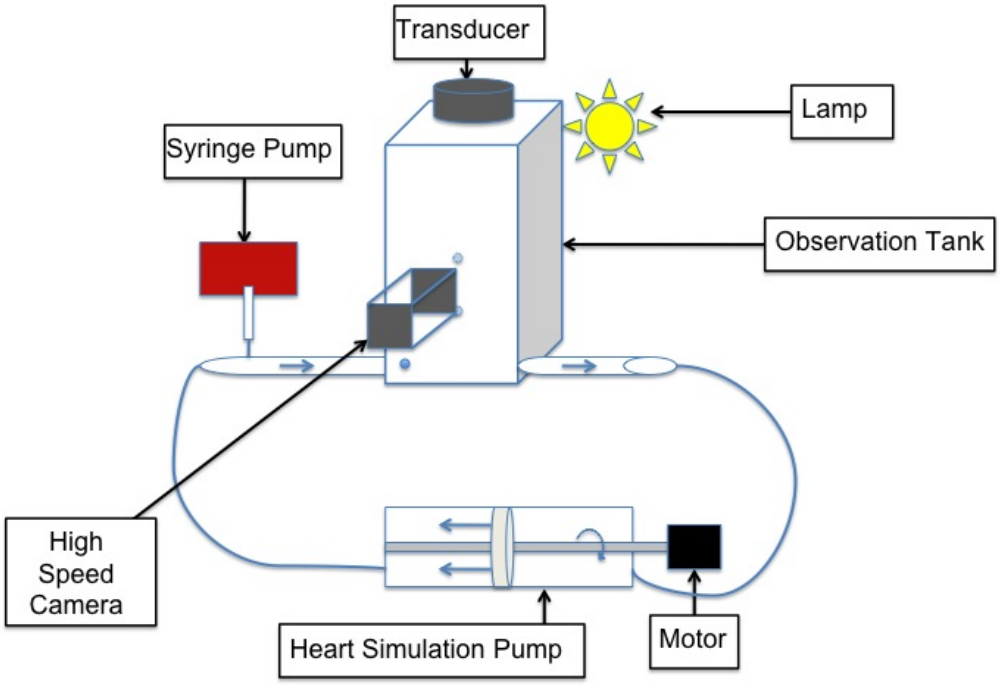

Figure 3.1: Experimental setup of open tank rising bubble experiments and the relationship between the major components in the experiment

3.1.1 Observation Tank

The observation tank used in the experiments has outside dimensions of 1 ft x 1 ft x 2 ft and is manufactured by Clear Cut Plastics in Seattle, WA. The walls (11/32 inches thick) are made of plastic, glued together with an epoxy. There are 5 holes in the tank. One is on the very bottom in the center. Two more are inset 2 inches from the outside edge of the front (camera side) of the tank and 2 inches from the outer edge of the bottom. The final 2 holes are located directly in the middle of the front and back of tank (6 inches from either outer edge) and 1 ft from the outer edge of both the top and the bottom of the tank. All the holes are large enough for a 3/8 inch tube fitting to fit through.

Water is used to fill the observation tank and is the medium through which the ultrasound travels until it reaches the microbubbles. Water, with an impedance of about 1.5 MRayls (similar to human tissue), offers the benefits of being transparent, cheap, having a known viscosity and density and readily available.

3.1.2 High Speed Camera

The visual data collection is handled by the Phantom 12 high speed camera. At the maximum resolution of 1280 x 800(200 μm x 125 μm), the camera is capable of taking pictures at frame rates just over 6,000 frames per second. At the minimum resolution, under ideal lighting conditions, the camera is capable of taking up to 1,000,000 image frames per second. With a 12 bit pixel depth and 6400 monochrome, 1600 color ISO sensor, the camera is still capable of saving just over 10,000 frames with its 8 GB memory.

3.1.3 Lens Configuration

The adaptor that connects the camera to the lens is the Tamron SP AF tele-converter. The Tamron SP Di lens (180 mm 1:3.5, macro 1:1) has a maximum aperture of 3.5 and is used at this setting throughout the experiment. This lens combination gives a 2:1 magnification at about 30 centimeters working distance. The optical resolution of this setup is about 10 microns per pixel.

3.1.4 Lighting

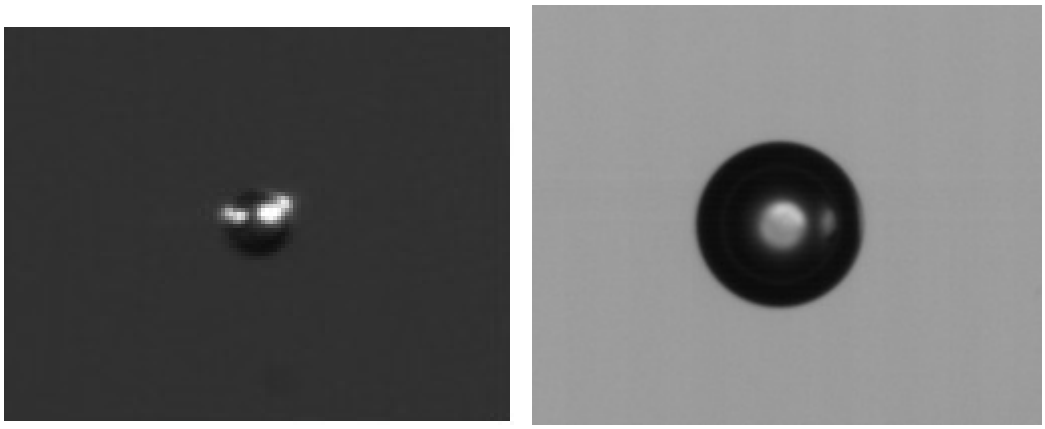

(a) Angle lit bubble

(b) Back lit bubble

Figure 3.2: With angle lighting and a dark background, bubble circumference is not colored homogeneously. However, bubble appears symmetric and circumference pixels all contain similar threshold values with a lamp directly behind the bubble

The position of the lamp is debatable due to the fact that bubbles and drops are usually photographed with a dark background with the illumination coming from either the top or one of the sides. Figure 3.2(a) shows a photograph of microbubbles with a dark background and light illuminating them from an angle. The photograph shows the sharp reflection of the lamp on the bubble surface. This is the typical image one thinks of when mentioning a bubble. However, the program that is used to find the diameter, center point and velocity of the microbubbles uses the threshold of each image pixel to process the photographs. Due to the large range of gray scales (ranging from dark black to light white) within the pixels that make up the bubble, it is nearly impossible to capture the true circumference. For this reason, the lamp is placed behind the bubble and the camera picks up the direct shadow of the bubble. Figure 3.2(b) shows the homogeneity of the pixels around the circumference of the bubble when this method is used. The ideal lamp for backlighting would be extremely bright and synchronized with the shutter of the

Figure 3.3: Lamp used for backlighting

camera. In lighting situations like this, the clarity of the image is very much dependent on the speed at which the camera is taking images and on the amount of light focused on the small field of view. The current lamp is a simple outdoor, 150 Watt lamp with a reflection cone that concentrates the light into the tank. Figure 3.3 shows the lamp used.

3.1.5 Transducer Controller

The transducer is controlled by an Olympus Panametrics-NDT Model 5077PR Squarewave Pulser/Receiver whose lowest and highest pulsing frequency settings are 100 kHz and 20 MHz respectively. Figure 3.4 shows the face of this control box (the settings shown are used in the first set of experiments measuring the rise velocity of microbubbles in an open tank).

Figure 3.4: Front face of control box that connects the transducer to the NI PCI-5114 card

(a) Birds eye view of transducer

(b) Transducer mount

Figure 3.5: Reson TC2116 transducer

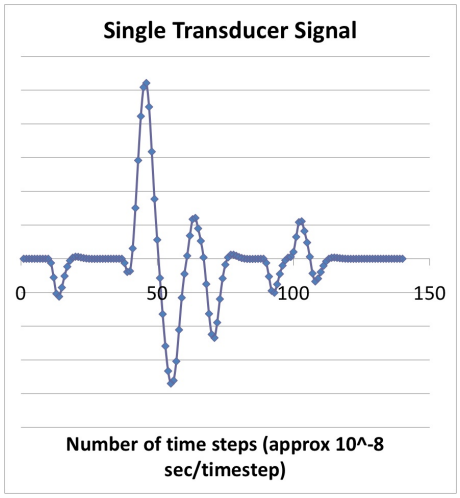

Figure 3.6: Transducer waveform data taken in Labview and graphed using the data points taken every 10^{-8} seconds.

3.1.6 Transducer

As mentioned above, the transducer is the main component of this experiment. The Reson TC2116 Broad Band High Power Transducer (see Figure 3.5) has an optimal operating frequency of about 50 kHz but it can be operated in the range between 40 and 100 kHz. The maximum input power is 1000W at 50 kHz 1% duty cycle and the beam width is about 13.5° (± 2°). It is about 17.78 cm in diameter and weighs 5 kg .

This particular transducer was chosen because the lower the frequency of the transducer, the larger the size of the resonance bubble (see Table 3.1). It is extremely hard to make air bubbles that are smaller than 100 μm, therefore, for this part of the experiment, the lower the transducer's frequency is, the better. The lowest frequency transducer found that did not have to be custom made was the Reson TC2116.

3.1.7 Acoustic Absorber Material

As the transducer emits its signal, the sound wave will bounce off of any surface it encouners as long as the impedance is less than infinity (figure3.7(b)). An acoustic absorbing

(a) Quash: Acoustic absorber

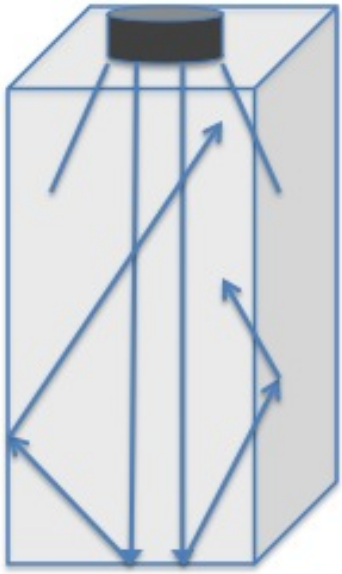

(b) Transducer reflections without the acoustic absorber

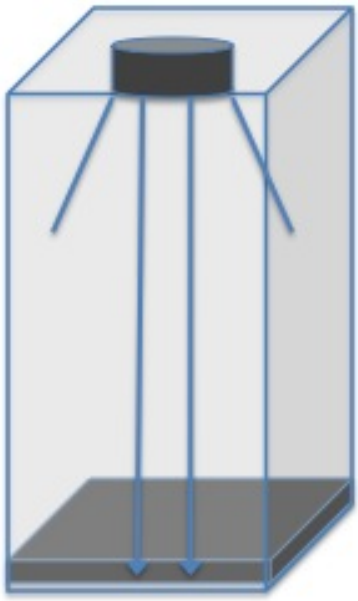

(c) Transducer reflections attenuated by acoustic absorber

Figure 3.7: Acoustic absorber justification

Table 3.1: Table of resonance bubble sizes determined by equation 2.1

Frequency (MHz)	Resonance Bubble Diameter (μm)
0.6	10.84
0.4	16.26
0.2	32.52
0.1	65.05
0.08	81.30
0.06	108.42
0.04	162.62

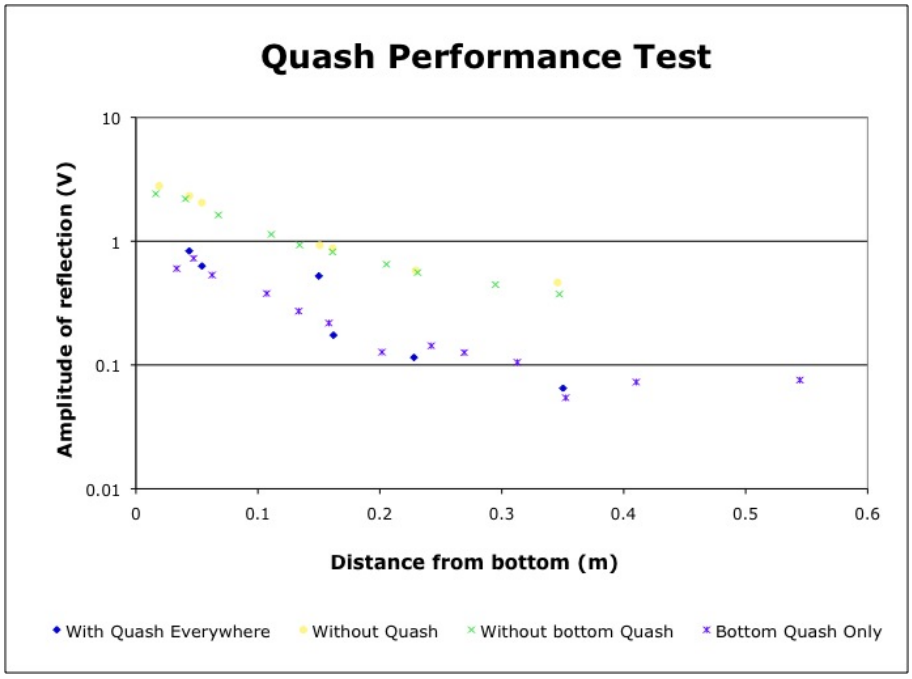

Figure 3.8: Independent axis is logarithmic and shows that the Quash material is very helpful in damping the amplitude of the reflection wave

material called Quash is tested (using a 1.0 MHz transducer) as a material which will minimize the reflected noise and therefore, the error in the rest of the data collection (figure 3.7(c). The amplitude of the reflection off the bottom of the tank is found at different heights from bottom of the tank. The tests are conducted with the Quash everywhere (bottom and sides), without the bottom (sides only), with only the bottom, and without the Quash at all. The results of these experiments are displayed in figure 3.8.

Figure 3.8 shows that the Quash material is most effective when it is on the bottom of the tank. The graph shows that having the Quash on the sides only does not significantly change the reflection amplitude. For this reason, the acoustic absorber is used on the bottom of the tank for all of the further data collection in this research.

3.1.8 Sound Field Data Collection

To determine the exact sound field of each transducer, a hydrophone (see Figure 3.10) and hydrophone positioning system (see Figure 3.9) are used. The hydrophone is from the Onda Corporation and is model HNC-1000 S/N 1061. The hydrophone comes with a preamplifier (AH 2020) and a DC block (AH 2020-DCBSW) that allows the user to add a gain to the acquired signal. This feature was not used in the measurements presented here.

The X-Y-Z positioning axes come from Velmex Incorporated. The aluminum tracks are coated with a lubricant and contain teeth that allow the positioning of each arm to be within 0.0635 centimeters accuracy. The X and Y axes of this particular system have a travel distance of 12.7 centimeters. This is sufficient because only one quarter of the tank needs to be mapped out since the transducer signal is axially symmetric. Although one side of the square tank is just over 27.94 centimeters, the arm that holds the hydrophone takes up half an inch of space so again, the 12.7 centimeter travel distance is sufficient. The Z axis has a travel length of 43.18 centimeters. This choice was made by considering the depth of the tank, the length required to classify the sound field, and the price of the device.

The extended arm shown in figure 3.9(b) was created to hold the hydrophone. The

(a) Entire positioning system

(b) Close-up of hydrophone holding-arm

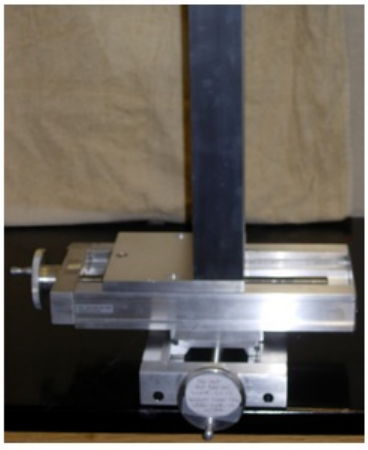

(c) Close-up of actuators

Figure 3.9: Hydrophone positioning system in its entirety, as well as close-ups of important parts

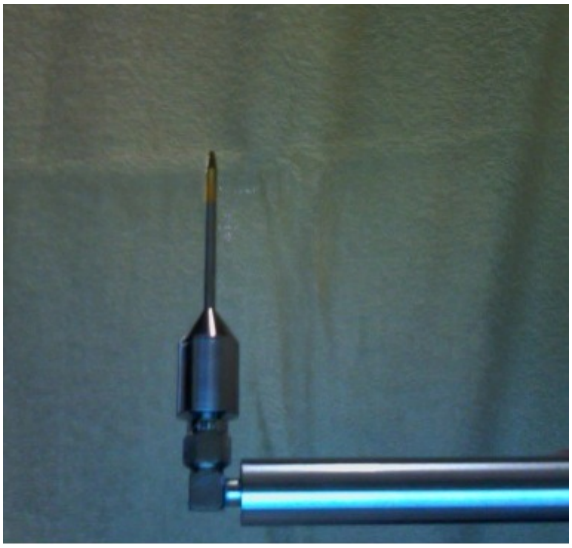

Figure 3.10: Onda hydrophone used for sound field acquisition

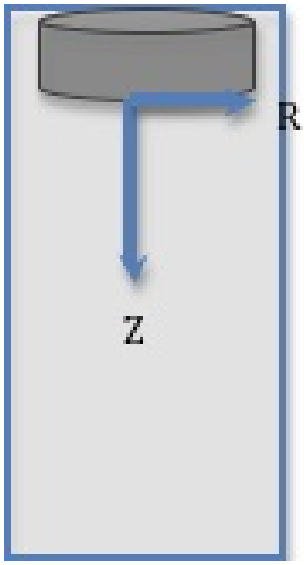

Figure 3.11: Acoustic field classification axes

hydrophone is held by this arm so that the tip is parallel to the sides of the tank and perpendicular to the flat, bottom surface of the transducer. The signal perceived by the hydrophone at z=0, x=0 and y=0 is the comparison point for all the other signals obtained throughout the tank. Because the transducer's signal is axially symmetric, the Cartesian coordinate axes X and Y can be transformed into the polar coordinate axis, R. Figure 3.11 shows the origin for all the data presented in the graphs below.

To measure the signal of the transducer at any given point in the observation tank, the PCI-5114 National Instruments card was used. Both the transducer and hydrophone signals are acquired by this fast-sampling (1,000,000 samples per second) data acquisition card. The signals are digitized with 12 bit precision and stored in text files for further analysis. The average amplitude for the 100 kHz transducer was measured at 0.015 volts which corresponds to a pressure amplitude of about 20,300 Pa.

Figure 3.12 shows the Labview front panel of a program that collects and stores the data from the transducer and hydrophone to be analyzed. This program is capable of taking analog data from the PCI-5114 card (channels 0 and 1) and saving a series of numbers that correspond to the value of the voltage experienced by the card. The sample rate, number of samples, and filter limits can be changed by the user as well as the initialization channels, and vertical range. The vertical range initialization is one of the most important aspects of this program. The acquisition card only has a set number of partitions it can use per channel to collect the data. By informing the card what the range of data is before taking it, the card can sort the data into these partitions as accurately as possible. The transducer and hydrophone lower limits are set to filter out any background noise that occurs within the signal. These values are determined by taking data when the devices are off and setting the noise maximum as each channel's filter limit. The time percentage offset is 2% because it is the lowest value Labview can handle without misinterpreting the incoming data. The file save format is set to six significant digits for accurate data collection. The description of how this interface was programmed can be seen in Appendix A.

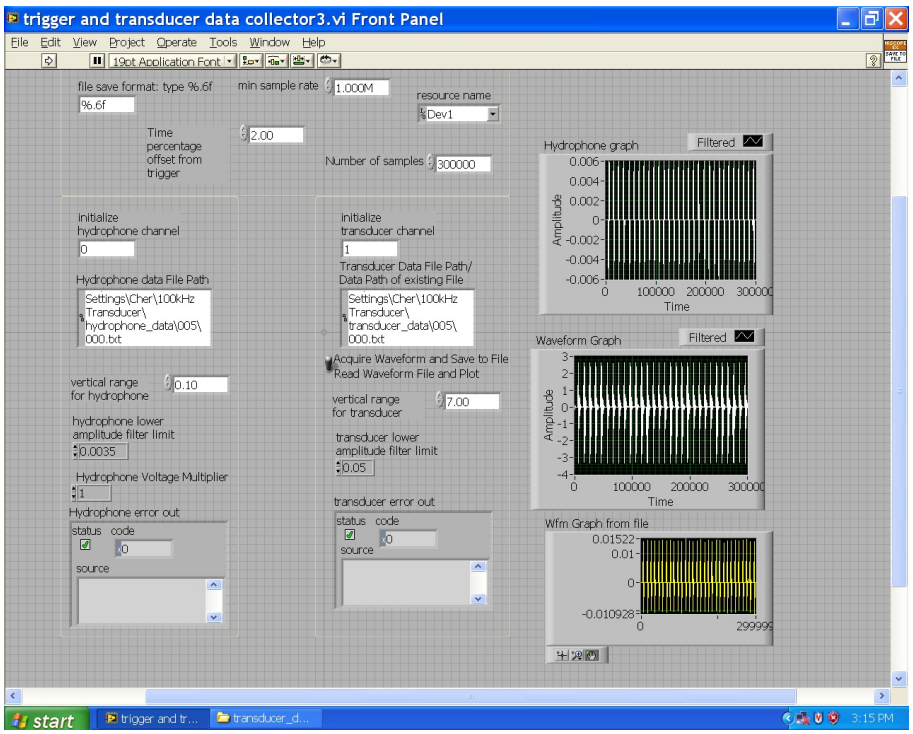

Figure 3.12: Front view of Labview file created to recieve signals from the transducer and hydrophone at the same time

3.1.9 Microbubble Creation and Injection

Although the chemically formulated UCAs are what's used in practice, their small size (3-12μm in diameter) makes them harder to manufacture and to capture on film. Therefore, only larger air bubbles (100-1000 μm in diameter) are used in the preliminary experiments which aim to verify the rise velocity of bubbles with and without the influence of ultrasound.

Two methods are used to create microbubbles that are injected into the open tank. The following section describes these methods and the possible three ways in which they may injected into the tank.

Pump and Syringe pump

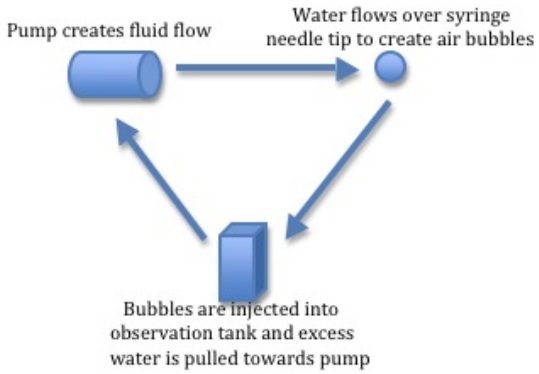

Figure 3.13: Flow diagram of fluid through system

The pump and syringe pump system described below is a recirculating system, therefore, the description will start and end on the same experimental device (figure 3.13). The heart simulation pump was originally created by undergraduates at the University of Washington in May of 2007. Figure 3.14 shows a close up view of the pump. The stepper motor which drives the pump is from Anaheim Automation and has high torque (1200 oz-in). The motor is controlled by the measurement and automation program from

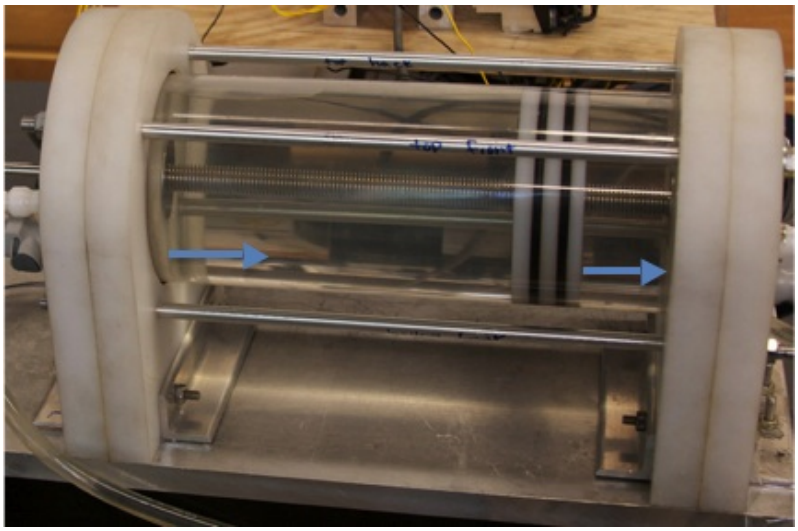

Figure 3.14: Fluid path through heart simulator pump

NI Instruments and the speed is determined by the number of steps per second the user requires. The details of the program, electrical equipment and mechanical equipment used to control the pump can be found in Appendix B.

The pump uses teflon for the two end sides and the piston itself, aluminum for the base plate and 4 support bars to hold the pump together, steel for the center threaded bar and the counterpart threaded nut attached to the piston, and clear plastic for the cylinder which guides the piston. There are also o-rings made of rubber that provide the sealing between the water on the two sides of the piston. The threaded rod in the middle of the pump drives the piston in its motion. The bar that goes from one side of the pump to the other and through the piston itself, keeps the piston from spinning on the center threads and forces the piston to instead translate laterally.

The pump needed many improvements throughout this project. First, the initial design relies on water to act as a lubricant. However, it is not nearly as good as an oil would be. Another large dilemma with the pump was the o-rings. When they have been sitting in water for more than a few hours, they retain water and expand. This also creates more

friction and can completely stop the motor. This problem was solved by trial and error of the exact size slots and o-rings that would keep the water from spilling over to the other side under pressure, but without stopping the motor.

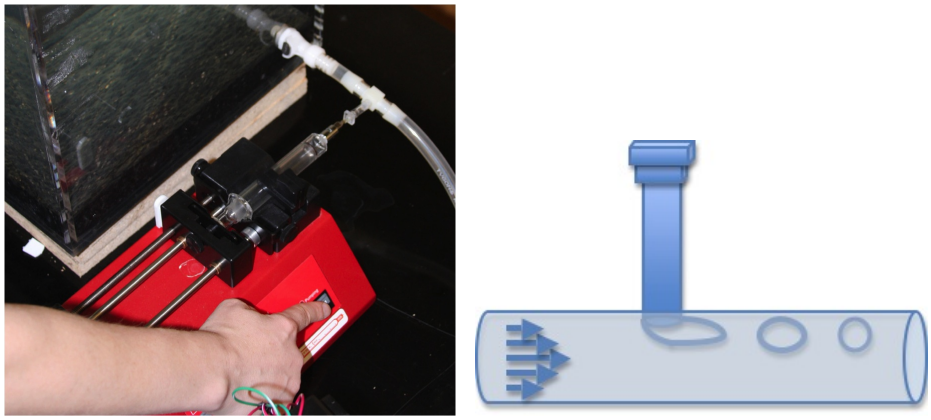

(a) Experimental setup of the syringe coming to a t-joint with the flow from the heart simulation pump.

(b) Flow past a needle pushing air into the stream creates bubbles. The size of the bubbles largely depends on the speed of the water flow, the speed of the air, and the inner diameter of the needle

Figure 3.15: Fluid past air injection system (syringe filled with air and injected through needle) creates bubbles

The pumped fluid enters into a tube of inner diameter 0.9525 cm. As the fluid passes through the Tygon ^{TM} R-3606 soft PVC tubing, it reaches the T-joint intersection where air is slowly pumped into the moving stream of water by the New Era Pump Systems, Inc. syringe pump, moving at a volume flow rate of approximately 1 mL/sec. Figure 3.15 shows how the air is injected at a 90° angle from the fluid flow. The force from the water pulls the air into the flow fast enough to overcome surface tension and create many small air bubbles. These bubble sizes are partially determined by the size of the needle attached to the syringe. In this case, the needle size is 22 gauge which gives an inner diameter of 0.413 mm.

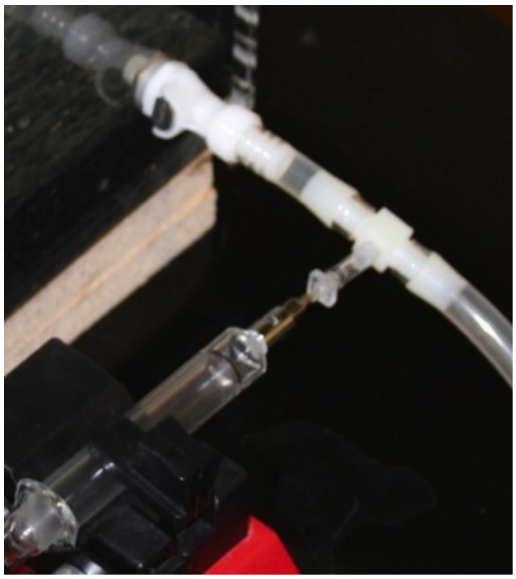

(a) Configuration #1: Low side entrance point

(b) Configuration #2: Middle side entrance point

(c) Configuration #3: Bottom center entrance point

Figure 3.16: The three places in which bubbles may enter the observation tank

The flow rate past the needle can be determined by using the speed of the motor and the distance between each thread on the center axis of the heart simulation pump. With a top speed of 5,000 steps per second, the flow rate past the needle is about 1000 cm^3/s. With an inner diameter of 0.9525 cm, the large scale Reynolds number for the tube in this situation should be about 95,000. However, due to the compressible air that is always trapped inside the heart simulation pump, it is possible that the Reynolds number is actually lower.

There are three options for introducing the bubbles into the tank. Figure 3.16 shows these three options and how the syringe pump is connected for each of them. When the bubbles enter through the high entrance, they are centered in the depth of the tank and are directed directly under the transducer. This option is also used later in the experiment for injecting the bubbles into a simulated artery (directed flow experiments will be discussed in the next chapter). The low entrance option injects the bubbles about two inches from the front of the tank (front being the side the camera lens is on). In the future, this will be the only option available for the true microscope lens because the focal distance is much shorter. This option used to be the furthest vertical distance from the transducer, which allowed the bubbles the longest amount of time to rise undisturbed by perturbances from the injection flow. Therefore, most of the data taken in the open tank observations was done using this entrance. However, after further investigation, a trend was observed (discussed in next paragraph) that prompted the creation of the final entrance point, the bottom entrance. The bottom entrance should have been the most optimal because it allowed the bubbles to rise directly under the center of the transducer and be the furthest from the transducer. However, because the syringe T-joint was directly under the hole, the bubbles never got a chance to break up into smaller bubbles before entering the tank. This problem may have been solved by speeding up the flow past the needle. Unfortunately, the friction in the pump was simply too high to allow for speeds any higher than they already were.

In the lower entrance, after taking a plethora of data, it was clear that external flow was effecting some of the bubbles. Figure 3.17(a) shows the approximate flow field that

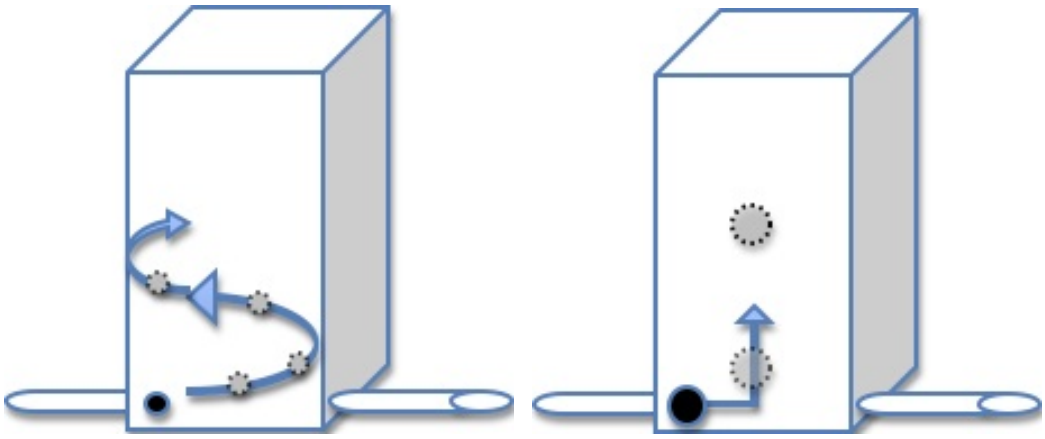

(a) Small bubbles ($O(10\ \mu\text{m})$) are effected by weak recirculation

(b) Large bubbles ($O(100\ \mu\text{m})$ are not effected by low velocity recirculation

Figure 3.17: Effect of weak jet stream on bubbles

effected bubbles with diameters below about 100 microns. The larger bubbles seemed to be unaffected, probably because their buoyancy forces overpowered any small perturbations in external flow. The results section presents the data in two types of graphs. The vertical rise velocity vs. diameter does not take into consideration these small perturbances. The total rise velocity includes the effects of the lateral movements of some of the bubbles due to the recirculation regions.

A similar Tygon $^{\text{TM}}$ tube is used to suck water from inside the tank to fill the other side of the heart simulation pump (Figure 3.14). The piston system is capable of pumping water in either direction. However, due to the configuration of the bubble injection system, the pump must be reset after reaching the end of the pump each time an experiment is conducted. Each experimental run takes approximately 45 seconds (depending on the pump speed) and captures one to two bubbles of the correct size (which may or may not be in focus). However, due to the sensitivity of the timing of the heart simulation pump, the syringe pump, the transducer, the lighting and the high speed camera trigger, only about one in every 5 trials provides usable data. The number of data points taken per day

is largely dependent on the time it takes to save the image files from the camera (usually about 10 minutes per bubble).

Waterfall Technique

After many uses, the observation tank becomes extremely dirty. To combat the growth of algae and other organisms, a Tetra whisper fish filter (Model 5-15 # 26308) was purchased which attaches to the top of the tank. This filter pulls water from the top of the tank, filters it, and ejects it back into the tank over a ledge that creates a small waterfall. The large droplets hit the surface of the water and simultaneously create air pockets as well as break up into smaller drops. The larger air bubbles quickly rise to the top of the tank, however, the smaller air bubbles ($O(100\mu m)$ or less) get forced down to the bottom of the tank. After a few minutes, there are hundreds of microbubbles. Upon unplugging the filter, the small flow field in the tank settles down and the small bubbles begin to rise. The transducer is turned on and the rising bubble images are captured with the high speed camera.

3.2 Bubbles Flow Perpendicular to Bjerknes Force

The following section describes the experimental components that are different from those found in the preliminary set of experiments. These components are specific to the experiments which measure the rise velocity of bubbles that are traveling in a flow that is perpendicular to the axis of the transducer. An overview of the setup for this set of experiments can be seen in figure 3.18.

The bubbles are pre-created using a solution for Ultrasound Contrast Agents found in Appendix C. The syringe pump is used to inject the bubbles into the tube as the flow inside the tube carries the bubbles in front of the camera. The bubbles are again imaged by the high speed camera, however, due to the especially small size of the UCAs used here, the lens must be changed out for a much more powerful one. Again, the bubbles are captured on film and stored in files that are later analyzed for rise velocity. The rest of this section describes the details of the specific components that are different from the

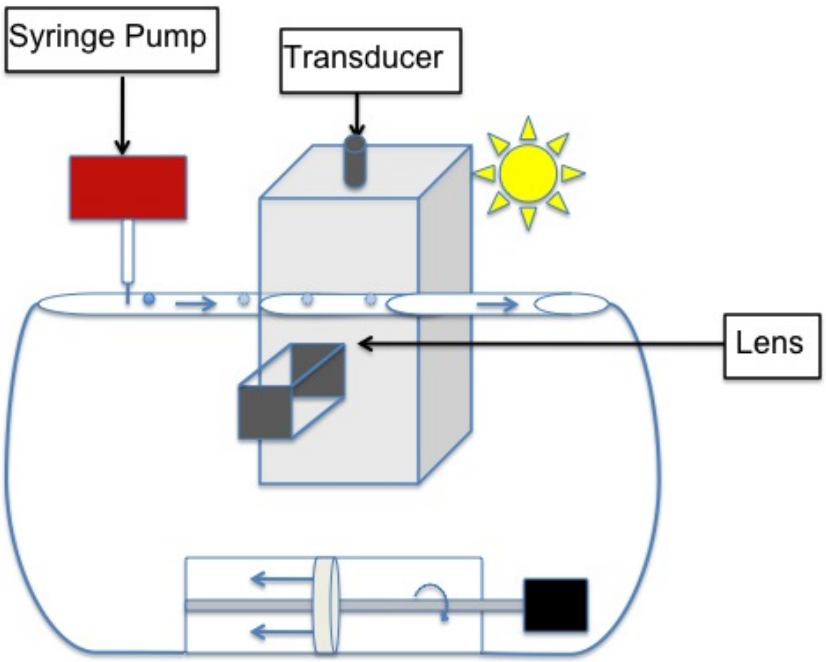

Figure 3.18: Experimental setup of open tank rising bubble experiments and the relationship between the major components in the experiment

first set of experiments.

3.2.1 Transducer

Due to the smaller size of the microbubbles used for this part of the experiment, a larger frequency transducer had to be used to manipulate the bubbles. The transducer used was a Panametrics-NDT V303, model 592249. The transducer was meant to be triggered at 1 MHz and was originally designed for Non-Destructive Testing (NDT). It is meant to have some water on the surface of a metal object and run over the top of it, reading the distance between the trigger signal and the reflected signal. For this reason, the optimal focus length of this transducer is between 1.524 and 2.032 cm. For our purposes, the transducer is used for the far field created well beyond the focal point.

3.2.2 Sound Field Inside Directional Tube

To determine the impedance through the tube that will channel the microbubbles in a unidirectional flow field, the pressure amplitude was sensed by the hydrophone both with and without the tube. Figure 3.19 shows the setup both with and without the unidirectional tube.

3.2.3 Lens Configuration

The lens used for this section of the experiments was a "Long Distance Microscope" manufactured by Infinity Photo-Optical Company in Boulder, CO. The model K2 lens has two extra TR Tubes that magnify the image 2x each. The total length of the lens is about 45.72 centimeters long and about 2.27 kg. Therefore, a special mount was created for both the camera and the lens so that each would be positioned and supported in the same exact location each day (figure 3.20).

(a) Without directing tube (b) With directing tube

Figure 3.19: Hydrophone test to find the relative difference in voltage recorded by labview between the water alone, and the water along with the tube which will direct the bubbles perpendicular to the transducer

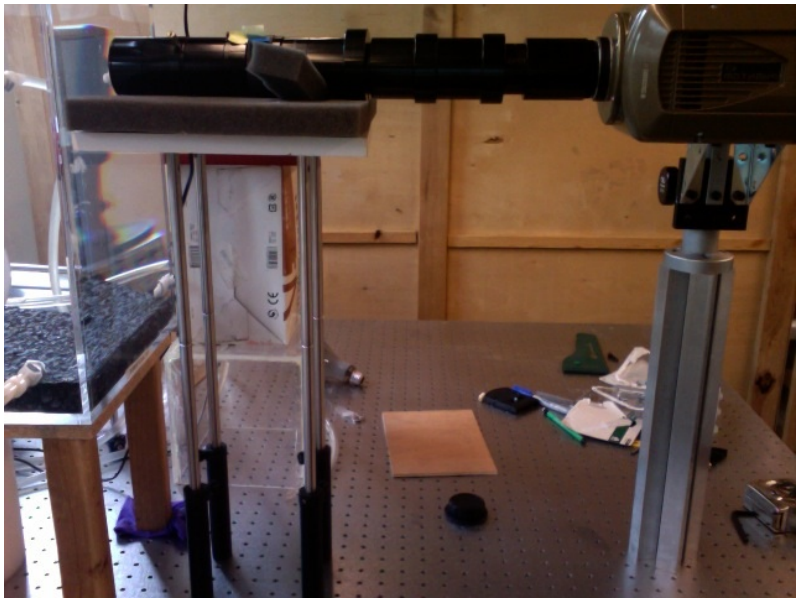

Figure 3.20: Support system for the camera and lens

3.2.4 Microbubble Creation and Injection

When the air bubbles were injected into the high entrance with the tube in place, there was no room for the bubbles to break up and become smaller. Instead, the bubbles were so large that they simply rose to the top of the tube and kept joining together to keep forming a larger and larger air pocket. In this case, the Reynolds number inside the tube was also chosen to be similar to that of the Reynolds numbers found in arteries. The ideal Reynolds number is just under 1000, which corresponds to a pump speed of about 10 steps per second. This slow speed (in comparison to the original speeds used in the previous section) was also not conducive to creating very small air bubbles.

However, another problem that arose when trying to create the ideal unidirectional flow situation was that the pump could not go below about 70 steps per second without getting caught by the static friction and pulsing instead of smoothly directing the water through the tubes. For this reason, most of the experiments were conducted at a speed of about 100 steps per second which corresponds to a large scale Reynolds number of about 1,400 inside the tube. In the previous section, a microbubble injection method was

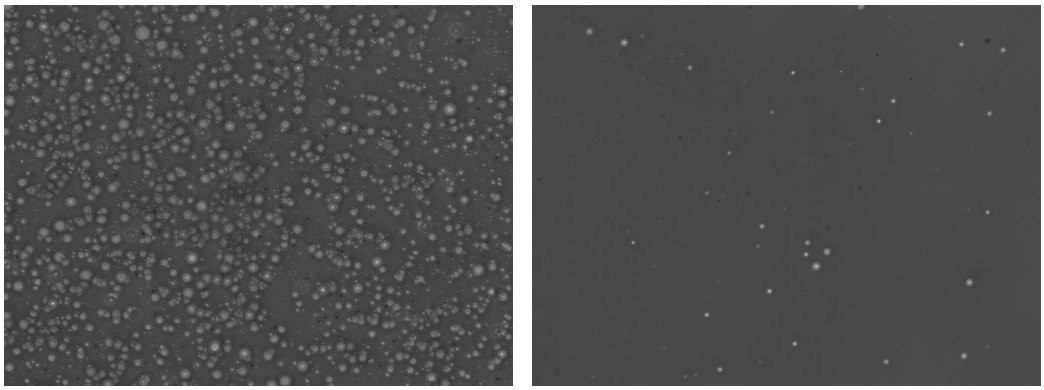

(a) Concentrated UCA solution (b) Diluted with 70% filtered water

Figure 3.21: Difference between concentrated UCA formula and diluted UCA formula

described that used the heart simulation pump along with air being slowly pushed out of

the syringe. Although, the pump speeds were too small to create bubbles in this fashion, the same technique was used to inject the already created UCAs into the high entrance of the observation tank. The ultrasound contrast agents are created using a lipid solution (details on the methodology can be found in Appendix C) and can survive as microbubbles even when injected into large volumes of water. Figure 3.21 shows the difference between the concentration of the UCA solution by itself and the concentration when 70% water is added. The diluted solution shows a large decrease in the concentration of the bubbles. However, it also shows that the bubbles are capable of withstanding a high concentration of water without dissolving. These bubbles are on average smaller than 10 microns and therefore, are extremely difficult to locate using the high speed camera. The perpendicular fluid flow experiment is a much better candidate for the use of these small bubbles because of the confined space that they must be maintained in.

Chapter 4

EXPERIMENTAL RESULTS AND ANALYSIS

The experimental results from both the open tank, and bubbles flowing perpendicular to Bjerknes force experiments are described in this chapter. The first section describes the pressure field in the tank when the 0.1 MHz (100 kHz) transducer is turned on. The second section describes the results from the open tank bubble injections and graphs the rise velocities both with and without the 100 kHz transducer. The third section describes the behavior of the bubbles when confined to a single flow direction that is perpendicular to the Bjerknes force created by the ultrasound transducer.

4.1 Transducer Pressure Field

The pressure field is different depending on the strength, mechanical configuration and precision of the transducer emitting the signal. Each particular transducer also emits a slightly different signal depending on the manufacturing conditions, and the precision of the technician who assembled it. For this reason the Reson TC-2116 transducer was tested with the Onda HNC-1000 hydrophone to determine the relative amplitudes of the pressure signals. The results are displayed in figure 4.1.

The graph plots the pressure field of the 0.1 MHz transducer measured by the hydrophone as a function of the radial distance from the center of the transducer. The colored lines represent the distance the tip of the hydrophone is from the surface of the transducer to the tip of the hydrophone (pointing downwards, located at the top of the tank). The colors go from red (closest to the transducer) to purple (furthest from the transducer).

The pressure wave produced by the transducer is felt by the piezo mechanism inside the hydrophone which converts the pressure into a voltage read by the PCI-5114 card.

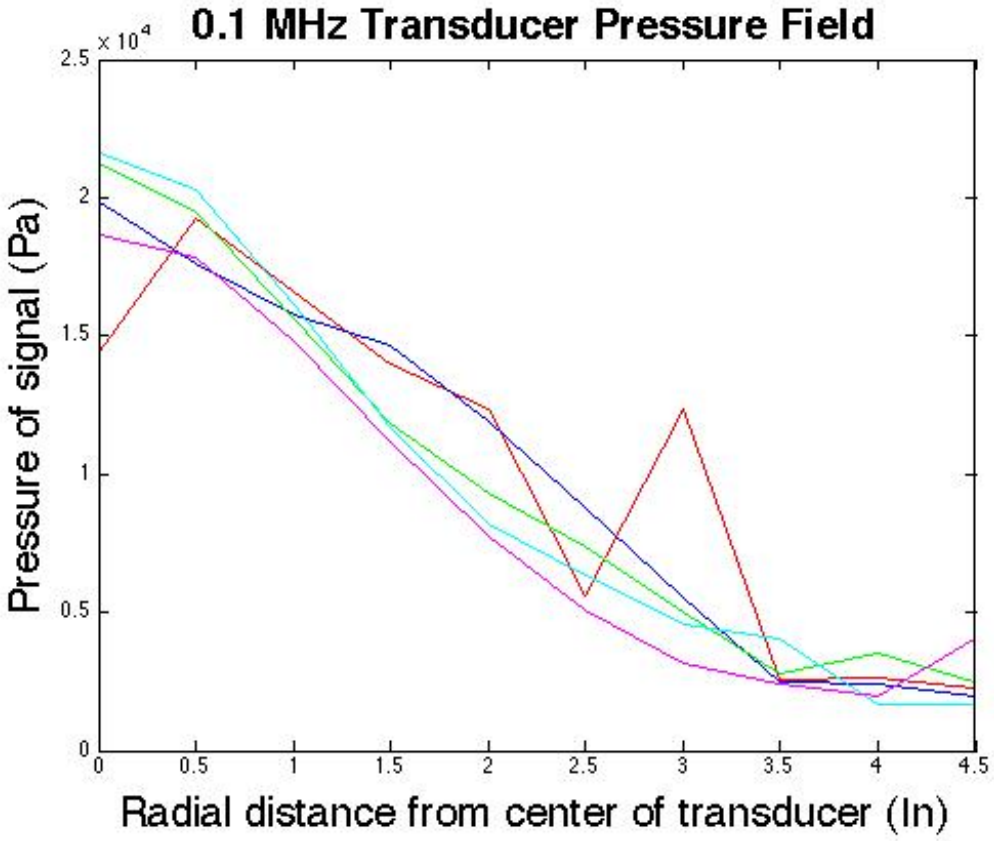

Figure 4.1: Colors indicate the distance in the Z direction from the transducer. The figure shows that the radial distance from the transducer effects the amplitude more than the depth

The labview program (figure 3.12) graphs the voltage and saves the data to a text file. The calibration of the hyrophone provides the correlation between the voltage and the true pressure. Therefore, the plot shows the amplitude of the pressure in pascals.

This graph shows that the radial distance from the center of the transducer effects the pressure amplitude much more than the axial distance. The signal is strongest about 7 inches from the surface of the transducer and in general, is weakest any further than about 13 inches from the transducer. Large fluctuations occur mostly between z=0.5 and z=1.0. These outliers probably exist because they are inside the focal length of the transducer. Towards the edges of the tank (past 3 inches from the center of the transducer), the signals are so similar that they overlap each other, regardless of the value of z.

4.2 Microbubble Rise Velocity (Open Tank)

4.2.1 Rise Velocity Measurements

The data stored by Labview as described in chapter 3, Section 1 (and Appendix B) is manipulated with an image processing software package developed by the National Institutes of Health called ImageJ. The data is split into two different graphs which represent different sized bubbles. One graph displays results from bubbles near the resonant diameter corresponding to the transducer used (about 65 μm for a transducer with frequency of 100 kHz). The second graph shows the difference between the vertical rise velocity of bubbles larger than 100 μm both with and without the transducer.

Figure 4.2 shows the relationship between the vertical rise velocity of the bubbles as a function of their diameter both with and without influence of the pressure wave created by the transducer. The first thing to recognize in this graph is that the lines present are simply meant to depict a general trend that the bubbles are following. In this case, the red line is higher than the blue line, which indicates a downward force imposed on the bubbles that were under the influence of the transducer. Another interesting thing to notice is the local minimum which occurs around bubbles with diameters near $65\mu m$, the resonant diameter for the 100 kHz transducer used in these experiments. This minimum

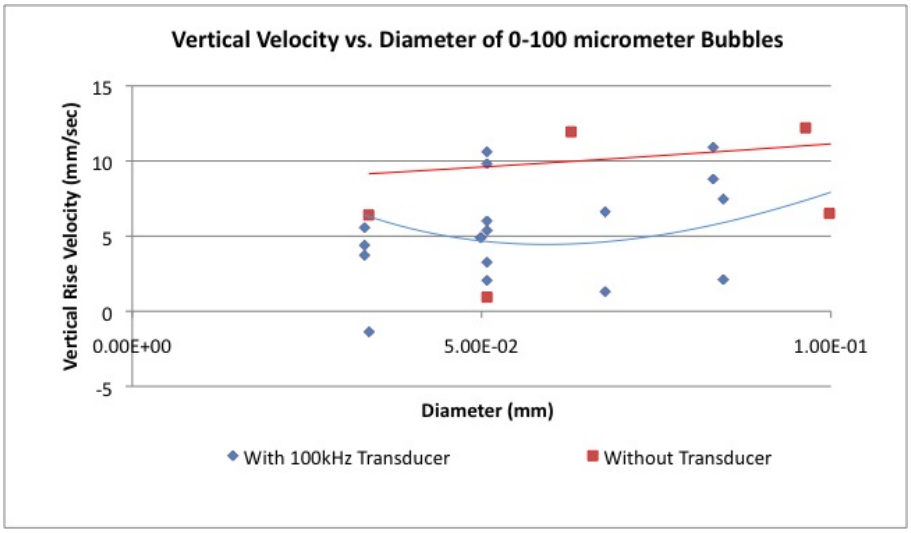

Figure 4.2: Vertical rise velocities of bubbles with diameters near 65 μm, the resonant diameter of the 100 kHz transducer. The red elements are uneffected by a pressure wave. The blue elements show bubbles under the influence of Bjerknes Force.

corresponds to a maximum Bjerknes force acting opposite the direction of the rise velocity.

Figure 4.3 shows a graph of the Bjerknes force as a function of $\frac{\omega_o}{\omega}$. This graph assumes a β_{tot} of 0.1[33] and a predetermined ω value of about 630000 which corresponds to the frequency of the transducer used here. The maximum force occurs when ω_o is equal to ω. Working backwards from a known omega found by the frequency of the transducer ($\omega = 2\pi F_{R_{transducer}}$), one may obtain the bubble radius which will create the corresponding ω_o ($1 = \frac{6\pi}{R_o(\omega)}$). The corresponding resonant bubble radius is near about 30 μm which corresponds to a resonant diameter near 60 μm, very close to agreeing with the original first order approximation found by equation 2.1.

From this discussion, it is now evident that bubbles with diameters near the resonant size that corresponds to the transducer being used should rise the slowest out of all the bubbles. The results show the blue curve below the red line for all bubble diameters. This is somewhat exaggerated by the line chosen, however, on average, the bubbles influenced

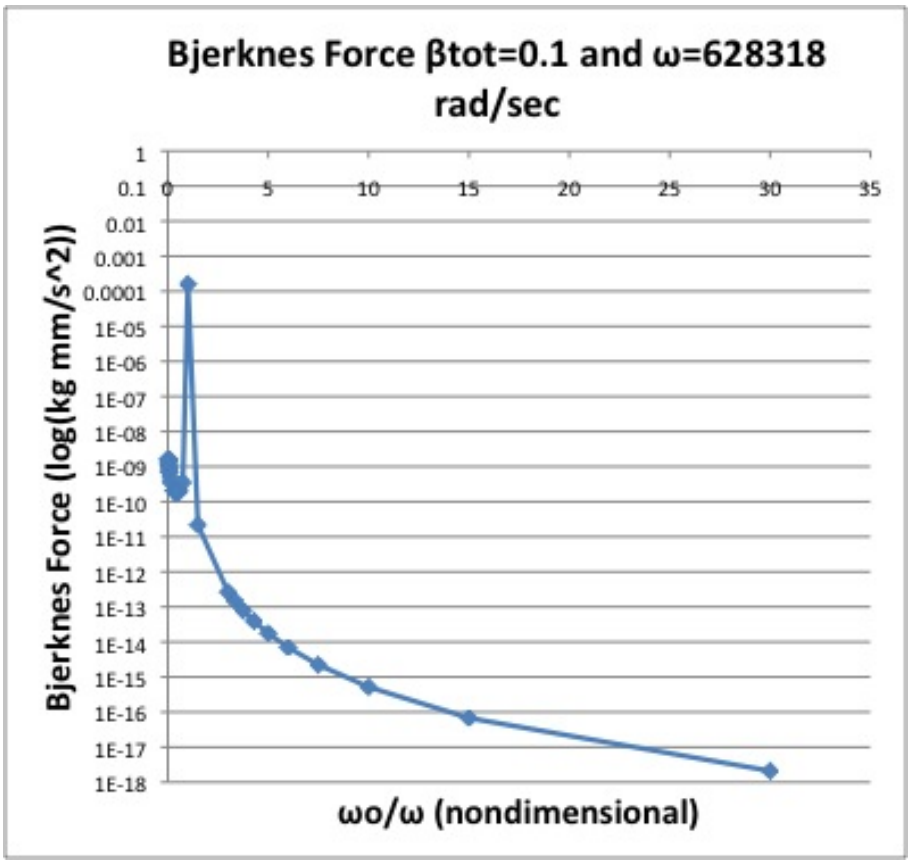

Figure 4.3: Bjerknes force as a function of ω_o (which is a function of bubble diameter) for a given transducer frequency. The maximum value of Bjerknes force is obtained when ω_o is equal to ω (predetermined by transducer used)

by the transducer do rise slower than the ones not influenced by the Bjerknes force.

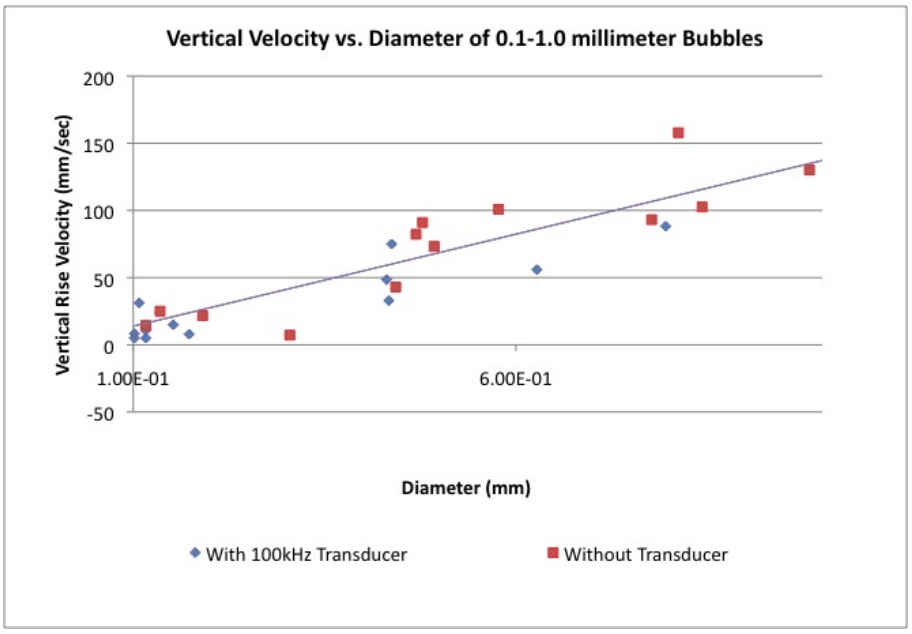

Figure 4.4: Vertical rise velocity vs. bubble diameters between 100-1000 μm. The red elements are uninfluenced by the pressure wave. The blue elements show bubbles that are under the influence of Bjerknes Force.

The other set of data describes the bubble dynamics of bubbles with diameters between 100 and 1000 μm. This data should not show a large difference between the points and fits because the resonance bubble diameter for the given transducer is not near these values. Figure **??** shows the relationship between the vertical rise velocity of the bubbles larger than 100 μm both with and without the influence of the 100 kHz transducer. The trend lines that are fit to these results show that there is very little difference between the trends of the red (without transducer) and blue (with transducer) data points. This is exactly what is expected for bubbles of this diameter.

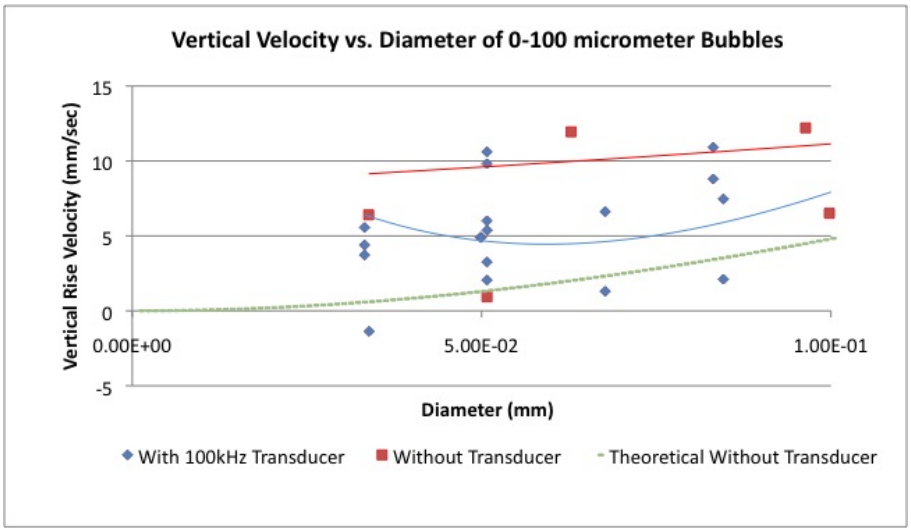

(a) Vertical rise velocity vs. bubble diameters between 0-100 μm

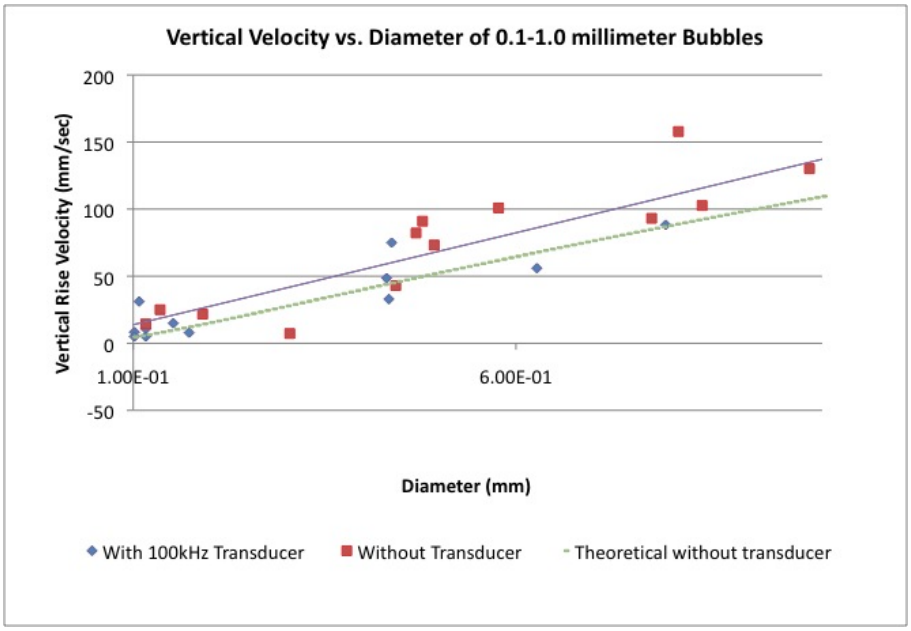

(b) Vertical rise velocity vs. bubble diameters between 100-1000 μm

Figure 4.5: The vertical rise velocity of all bubble sizes compared with the theoretical values. Green fit corresponds to the theory that corresponds to bubbles without the influence of the transducer. The red elements are uneffected by a pressure wave. The blue elements show bubbles that are under the influence of Bjerknes Force.

4.2.2 Comparison With Theory

The theoretical values that are obtained in figure 4.5 are found using equation 2.26. The equation is used without the Bjerknes force because there are factors such as B_{tot} that are unknown and would therefore not provide a good estimate.

There are two reasons that the theory under-predicts the experimental data. In general, the drag coefficient used for the theoretical curve assumes that the water is fully contaminated (either by particles, or solvents. $\frac{24}{Re}$ is a very high estimate for the drag coefficient (where high drag coefficients correspond to slow rise velocities). For pure water, with no contamination, the drag coefficient can easily be as little as $\frac{16}{Re}$, which still only splits the difference between the current theoretical trend and the most of the experimental data points. However, another effect that can lower the drag coefficient even further is anything that raises the Reynolds number. As stated in chapter 2, this Reynolds number uses the total velocity of the bubbles in the tank. Although the bubbles with large horizontal velocities were eliminated before the data was analyzed, all of the bubbles still have some horizontal velocity component that would effect the total drag coefficient. Also, it is possible that since the velocity inside the tube for these experiments is so large (about 1000 cm^3/s), it may induce transitional turbulence, creating a higher large scale Reynolds number inside the tank, which would break up the water and allow the bubbles to rise faster.

4.3 Bubble Dynamics in Unidirectional Flow Perpendicular to the Bjerknes Force

The bubbles used for these experiments are the UCAs described in Appendix D. The results in this section are given by grouping the bubbles and averaging their rise velocity based on two things: their size and their location within the tube. The decision to group the bubbles based on their size was made by the fact that the resonant diameter which corresponds to the transducer used for these experiments (1 MHz) is about 6 μm and this falls near the center of the bubble sizes that were studied. The bubble sizes fall into three categories: between 2 and 5 microns in diameter, between 6 and 9 microns in diameter,

and larger than 9 microns in diameter. At least 5 bubbles are averaged for each point on the graph.

The motivation for dividing the flow phantom tube into three sections comes from the idea that in a constrained flow such as this, the bubbles are affected by an additional shear force that is the largest near the tube walls.

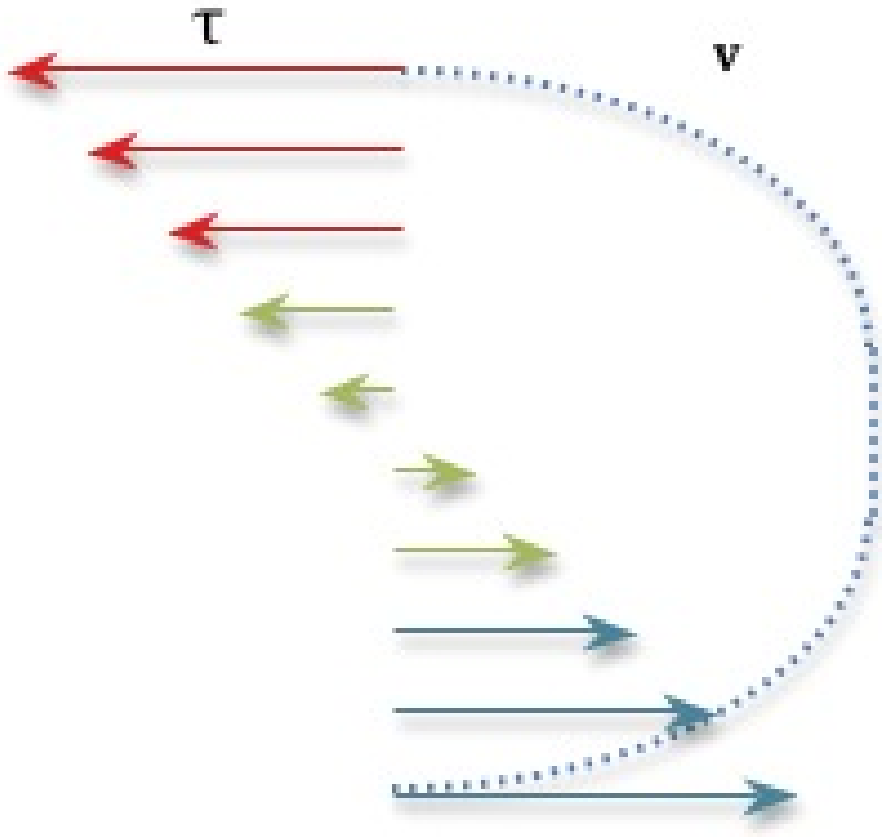

Figure 4.6: Shear resulting from Poiseuille flow in tube. The shear which imposes the Saffman force is always largest near the walls.

Figure 4.6 color codes the three sections that the data is broken up into based on its location within the tube. Bubbles located in the top third of the tube, indicated by

red graphical elements, will spin counter-clockwise due to the fact that the velocity on the bottom of the bubble is larger than the velocity on the top of the bubble. However, bubbles in this region are spinning faster than the bubbles in the center of the tube and therefore will be more effected by the Saffman lift regardless of which direction they are spinning .

Bubbles located in the center of the tube are marked by green points in the following graphs. These bubbles are least effected by the Saffman lift due to the small amount of shear experienced in the center of the tube. Finally, the bubbles colored blue are located on the bottom of the tube and spin clockwise.

The data is presented in graphs that describe the location of the bubbles based on the pixel location in the camera sensor. The center of the tube (r=0 μm)corresponds to a pixel location of Y=-300. The top and bottom of the sensor correspond to Y=0 (r=625 μm) and Y=-600 (r=625 μm) respectively.

Poiseuille flow is characterized by steady, fully developed flow in a pipe where the no slip condition at the walls creates a maximum flow velocity in the middle of the pipe and minimum flow velocities on the walls of the pipe. Shear (τ is defined as the dynamic viscosity of the liquid multiplied by the difference of the velocity over the difference in y ($\tau = \mu \frac{du}{dy}$). The larger the velocity difference acting on the top and bottom of the bubble, the larger the shear affecting the trajectory of those particles is. Since Poiseuille flow is described by a parabola, the largest velocity slope is near the walls.

4.3.1 Average Rise Velocities Without Effects of Transducer

FIgure 4.7 shows the total average of all the sections in the dark blue line with the diamond for a marker. The total average is around 0.225 mm/s for bubbles between 2 and 5 μm, 0.3 mm/s for bubbles between 6 and 9 μm, and 0.34 mm/s for bubbles above 10 μm in diameter.

In agreement with theory, the bubbles with the smallest diameter rise the slowest. Also, the total average rise velocity is 0.291 mm/s, which is shown to be higher than the total average rise velocity of bubbles influenced by the ultrasound pressure wave in the

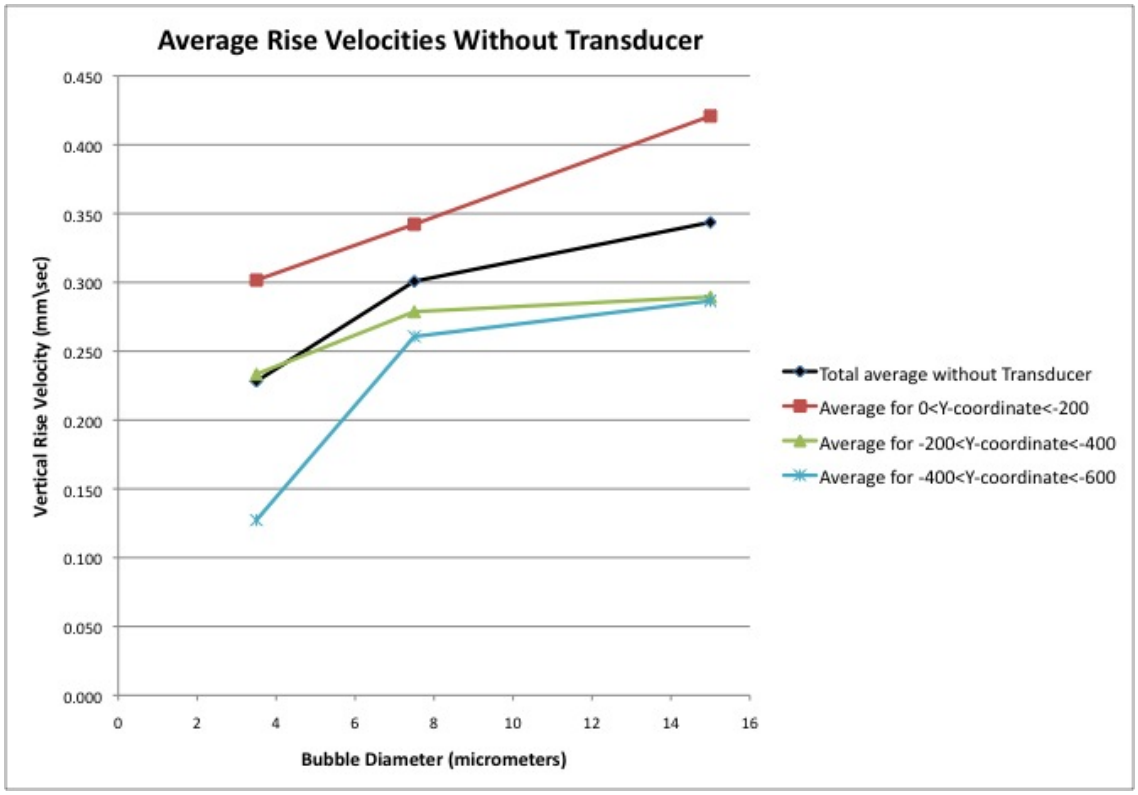

Figure 4.7: Effects of the unidirectional flow that is perpendicular to the axis of the transducer.

next section.

Another thing that is important to notice in this graph is that the rise velocity of the bubbles in the top third of the tube rise significantly faster than the average rise velocity of bubbles without the influence of the transducer. Even more significant is the separation between the rise velocities of the bubbles located in he top third of the tube compared to the bubbles located in the bottom third of the tube.

The speculation for why this is true is due to the Saffman force imposed on spinning spheres at low reynolds numbers that are subjected to shear flows. The Saffman lift is applicable in this situation because $Re_{\dot{\gamma}} < 0.1$. In this case, the shear rate is estimated to be 3.52 1/s with a kinematic viscosity of $10^{-}6\frac{m^2}{s}$ and an average bubble diameter of about 8 μm, which gives $Re_{\dot{\gamma}} = 0.000208$. The Saffman force could be solved analytically for each bubble in the data set (based on its particular radius, distance from the center of the tube, mean velocity of flow in the tube, and velocity difference between the bubble and the flow around it), however, this is nearly impossible to actually carry out because of the need for the relative velocity. Although this force cannot be calculated with the data obtained here, it can be analyzed as a whole.

In this case, it is evident by the description in Saffman's paper that bubbles traveling faster than the fluid they are in will be forced away from the center of the tube. This is the case observed in figure 4.7. The bubbles located in the top third of the tube rise at a much faster velocity than those which reside in the bottom third of the tube. This is due to the inertial forces pushing up on the bubbles in the top third of the tube and pushing down on the bubbles in the bottom third of the tube.

4.3.2 Average Rise Velocities with Influence of 1 MHz Transducer

One trend that is important to notice in figure 4.8 is that the average rise velocities of the small, medium and largest bubbles are around 0.154, 0.217 and 0.288 mm/s respectively. These values are all lower than the average rise velocity of the bubbles that are not influenced by the transducer. These values are significantly lower than the averages without the transducer. This shows that the transducer is certainly creating an additional

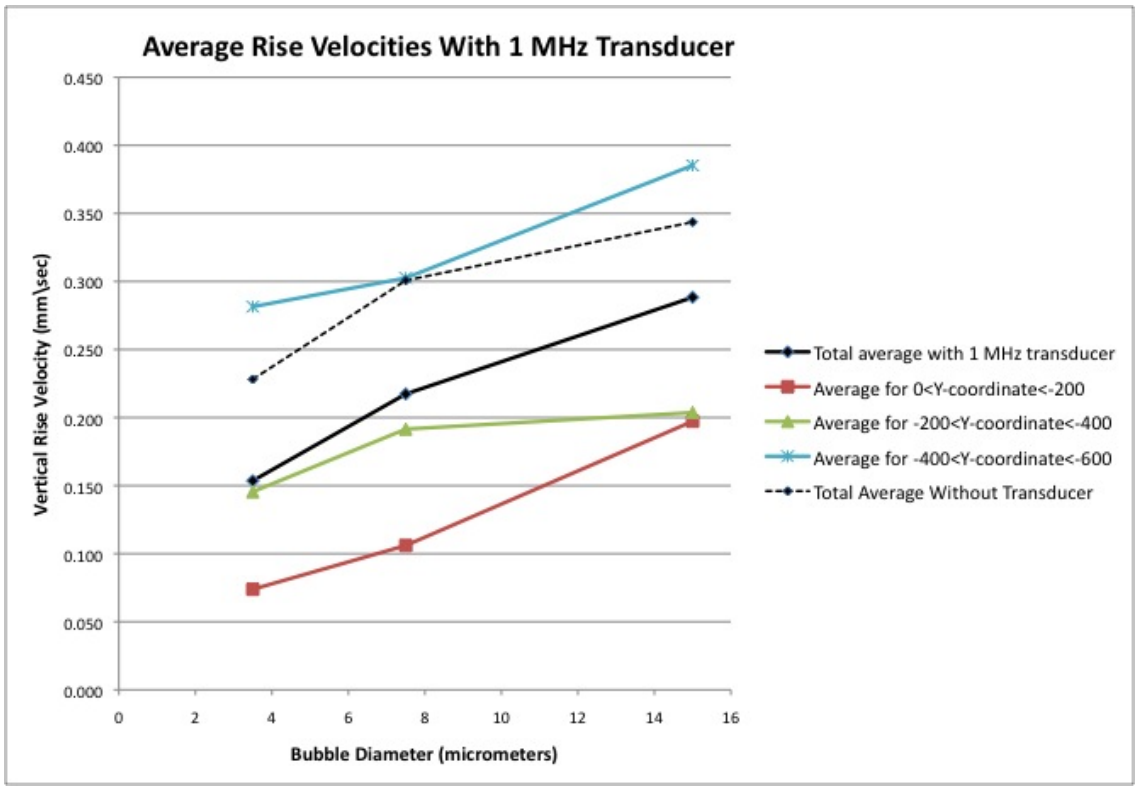

Figure 4.8: Effects of the unidirectional flow that is perpendicular to the axis of the transducer with bubbles under the influence of the 1 MHz transducer.

downward force on the bubbles.

Another important feature of this graph, and probably the most interesting phenomenon which occurs in these experiments, is the fact that the bubbles located in the top third of the tube now rise significantly slower than the average and even more significantly slower than the bubbles located in the bottom third of the tube. Slight changes in the dynamics of the bubbles can change the direction of the force, based on the difference between the velocity of the bubble and the fluid flow. The most commonly understood way to flip the force is to change the speed of the spherical particles with respect to the speed of the flowing liquid. In this case, the direction of the Saffman force being toward the center of the tube implies that the bubbles are slowed down so that their relative velocity is less than the velocity of the fluid particles around them. This slow-down is most likely caused by the oscillations of the bubble volume.

In general there are some sources of uncertainty which could affect the data that shown in the previous plots. The camera focal plane is not always directly on the center of the tube. Variations in the speed of the pump occur due to imperfections in the manufacturing and filling process. The bubbles should be far enough apart from each other not to influence each other, it is also possible that if there is a bubble directly below another bubble (or two or three), the effect of the transducer could induce secondary Bjerknes forces. The length of time the pump was running before the data was taken could also influence the experiments. This would determine how fully developed the Poiseuille profile is matched inside the tube. However, these possible errors were considered early on in the experiments and avoided as much as possible. Finally, the data was processed manually because the contrast between the background and the bubbles was not large enough for the ImageJ software to process. Therefore, there is some operator uncertainty due to the subjectivity of the bubble positioning. All the results have an error of at least $\pm$ one pixel which is .002 mm or 2 microns.

Chapter 5

CONCLUSIONS AND RECOMMENDATIONS

This chapter reviews the conclusions and possible future work that has come out of the experiments carried out in the current research. The first section recaptures the most important observations and states the conclusions made based on these observations. The second section describes some experimental recommendations that should be considered in the continuation of this project as well as the next major steps that should be carried out in future experiments relating to this work.

5.1 Conclusions

5.1.1 Open Tank Rise Velocity Experiments

Overall, the data showed what was expected from theory. When the transducer was introduced, the rise velocities of the bubbles near resonant diameters were significantly reduced. The rise velocity of the bubbles in all cases were larger than the theory (equation 2.25) predicted due to the fact that the Reynolds numbers in real applications are always higher than those predicted in theory. The water used for most of the experiments was either filtered or distilled, so the lack of contamination would increase the rise velocity. Although the flow in the open tank caused by the recirculation from the jet stream that created the bubbles is not fully classified, it is known that all of the bubbles were slightly effected by a horizontal velocity component that would also raise the total Reynolds number and lower the drag coefficient (raising the rise velocity).

5.1.2 Unidirectional Flow Perpendicular to Bjerknes Force Rise Velocity Experiments

The UCAs used in this portion of the experiment provided a means for obtaining data for much smaller bubble sizes. These experiments showed that the average rise velocities

of the bubbles without the influence of the transducer were about 25% higher than those under the influence of the 1 MHz transducer. The rise velocities of the bubbles close to the resonance diameter (about 6 μm) rose 30% slower with the influence of the corresponding resonant frequency pressure wave.

The Saffman force was evident in the results from these experiments. Without the transducer, deductive reasoning shows that the bubbles traveled slightly faster than fluid particles around it because the inertial effects from the shear forced the bubbles toward the outside of the tube. When the transducer is turned on, the rise velocity of the bubbles on the bottom third of the tube is significantly higher than those bubbles located in the top third of the tube. Here, the Saffman lift has switched directions due to the slowing of the bubbles, with respect to the fluid around them, caused by the oscillations in the bubble volumes.

5.2 Recommendations for Future Research

To accomplish the overall goal of being able to control microbubbles inside any given artery, certain steps could be taken to have the microbubbles interact with a more realistic environment. Human arteries do not have perfectly smooth walls. The shape of the tube used should have the same bumps of endothelial cells and be able to deform slightly with the change of liquid pressure inside. Because the carotid bifurcation is of importance in the treatment for stroke, this research could also benefit from a realistic bifurcating artery. The dynamics of microbubbles transferring from high-flow to low-flow using the Bjerknes force will be much different from the current research and should be investigated further.

Another important step in this research is to program the pump to create a fluid velocity profile that behaves like the pulsing blood in an artery. Theoretically it would require a much more complicated analysis, as the flow changes from Poiseuille type to Womersley type. This is a difference that will also greatly change and complicate the dynamics of the microbubbles with and without the use of the ultrasound transducer. This has never been attempted before and will probably provide some of the most important results this research will accomplish in the long run.

BIBLIOGRAPHY

[1] V. Bjerknes. Fields of force. 1906.

[2] E. Brujan, G. Keen, A. Vogel, and et al. The final stage of the collapse of a cavitation bubble close to a rigid boundary. *Physics of Fluids*, 14(1):85–92, 2002.

[3] L. Crum and A. Eller. Motion of bubbles in a stationary sound field. *Journal of Acoustical Society of America*, 48(2):181–189, 1969.

[4] L. Crum and A. Eller. Motions of bubbles in a stationary sound field. *Journal of Acoustic Society of America*, 48(1):181–189, 1970.

[5] K. Darge, J. Troeger, T. Duetting, and et al. Reflux in young patients: Comparison of voiding us of the bladder and retrovesical space with echo enhancement versus voiding cystourethrography for diagnosis. *Radiology*, 210(1):201–207, 1999.

[6] S. Datta, C. Coussics, A. Ammi, and et al. Ultrasound-enhanced thrombolysis using definity(r) as a cavitation nucleation agent. *Ultrasound in Medicine and Biology*, 34(9):1421–1433, 2008.

[7] K. Davis, D. Widder, and J. Taveras. Assessment of ventricular shunt patency by sonography: A new noninvasive test. *American Journal of Roentgenology*, 147:353–356, 1986.

[8] A. Eller. Force on a bubble in a standing acoustic wave. *Journal of Acoustical Society of America*, 43(1):170–171, 1968.

[9] S. Jibril F. Degenhardt and B. Eisenhauer. Hysterosalpingo-contrast sonography (hycosy) for determining tubal patency. *Clinical Radiology*, 51(12):893–896, 1996.

[10] S. Feinstein, J. Cheirif, F. Cate, and et al. Safety and efficacy of a new transpulmonary ultrasound contrast agent: Initial multicenter clinical results. *Journal of the American College of Cardiology*, 16:316–324, 1990.

[11] S. Fujikawa and T. Akamatsu. Effect of the non-equilibrium condensation of vapour of the pressure wave produced by the collapse of a bubble in a liquid. *Journal of Fluid Mechanics*, 97(3):481–512, 1980.

[12] L. Hoff and N. Dejong. Ultrasound scattering properties of albunex microspheres. *Ultrasonics*, 31(3):175–181, 1993.

[13] V. Kamath and A. Prosperetti. Numerical integration methods in gas bubble dynamics. *Journal of the Acoustical Society of America*, 85:1538–1548, 1989.

[14] A. Killam, B. Ito, B. McFerran, and et al. Functionally significant coronary stenosis determined with the combined use of the ultrasound contrast agent s069 and the stress agent arbutamine in the conscious canine. *Circulation*, 94(8):2622, 1996.

[15] P. Krishna and V. Newhouse. Second harmonic characteristics of the ultrasound contrast agents albunex and fs069. *Ultrasound in Medicine and Biology*, 23(3):453, 1997.

[16] I. Langmuir and K. Blodgett. A Mathematical Investigation of Water Droplet Tradjectories.

[17] W. Lauterborn. Laser-induced cavitation. *Acustica*, 31(2):51–78, 1974.

[18] T. Leighton. *The Acoustic Bubble*. Academic Press, 1994.

[19] T. Leighton, A. Walton, and M. Pickworth. Primary bjerknes force. *Eur. J. Phys.*, 11:47–50, 1990.

[20] Minnaert M. On musical air bubbles and sounds of running water. *Phil Mag*, 16:235–248, 1933.

[21] Y. Matsumoto and S. Yoshizawa. Behaviour of a bubble cluster in an ultrasound field. *International Journal for Numerical Methods in Fluids*, 47(6-7):591–601, 2005.

[22] H. Mitome. Micro bubble and sonoluminescence. *Japanese Journal of Applied Physics*, 40:3484–3487, 2001.

[23] A. Najafi, Z. Xu, and J. Mashyah. Single micro-bubble generation by pressure pulse technique. *Chemical Engineering Science*, 63(7):1779–1787, 2008.

[24] R. Nigumatulin, N. Khabeev, and F. Nagiev. Dynamics, heat and mass transfer of vapor gas bubbles in liquid. *International Journal of Heat and Mass Transfer*, 24(6):1033–1044, 1981.

[25] G. Poe and A. Acrivos. Closed streamline flows past rotating single cylinders and spheres-inertia effects. *Journal of Fluid Mechanics*, 72(12):605–623, 1975.

[26] H. Poritsky, 1952.

[27] P. Saffman. The lift on a small sphere in a slow shear flow. *Journal of Fluid Mechanics*, 22:385–400, 1965.

[28] F. Takemura and Y. Matsumoto. Influence of internal phenomena of gas bubble motion (effect of transport phenomena and mist formation inside bubble in the expanding phase). *JSME International Journal*, B-37(4):736–745, 1994.

[29] R. Tong, W. Schiffers, S. Shaw, J. Blake, and D. Emmony. The role of 'splashing' in the collapse of a laser-generated cavity near a rigid boundary. *Journal of Fluid Mechanics*, 380:339–361, 1999.

[30] W. Wang, H. Ding, Q. Qi, and et al. Characterization of focal hepatic lesions with contrast-enhanced c-cube gray scale ultrasonography. *World Journal of Gastroenterology*, 9(8):1667–1674, 2003.

[31] M. Wheatley, B. Schrope, and P. Shen. Contrast agents for diagnostic ultrasound: Development and evaluation of polymer-coated microbubbles. *Biomaterials*, 9:713–717, 1990.

[32] D. Widder and J. Simeone. Microbubbles as a contrast agent for neurosonography and ultrasound guided catheter manipulation: In vitro studies. *American Journal of Roentgenology*, 147:347–352, 1986.

[33] Z. Zhang and H. Zhang. Surface tension effects on the behavior of a cavity growing, collapsing, and rebounding near a rigid wall. *Physical Review E*, 70.

[34] Y. Zhao and S. Cho. Micro air bubble manipulation by elecrowetting on dielectric (ewod): Transporting, splitting, merging and eliminating of bubbles. *Lab on Chip*, 7(2):273–280, 2007.

Appendix A

BLOCK DIAGRAM OF LABVIEW DATA ACQUISITION FILE

This appendix will explain the coding of the labview file created to take the data from the PCI-5114 card and store it to text files. The block diagram shown in figures **??** and **??** will be referred to throughout the rest of this appendix. The block diagram for the labview file created to take the data from the PCI-5114 data acquisition card is shown in the Figures **??** and **??**.

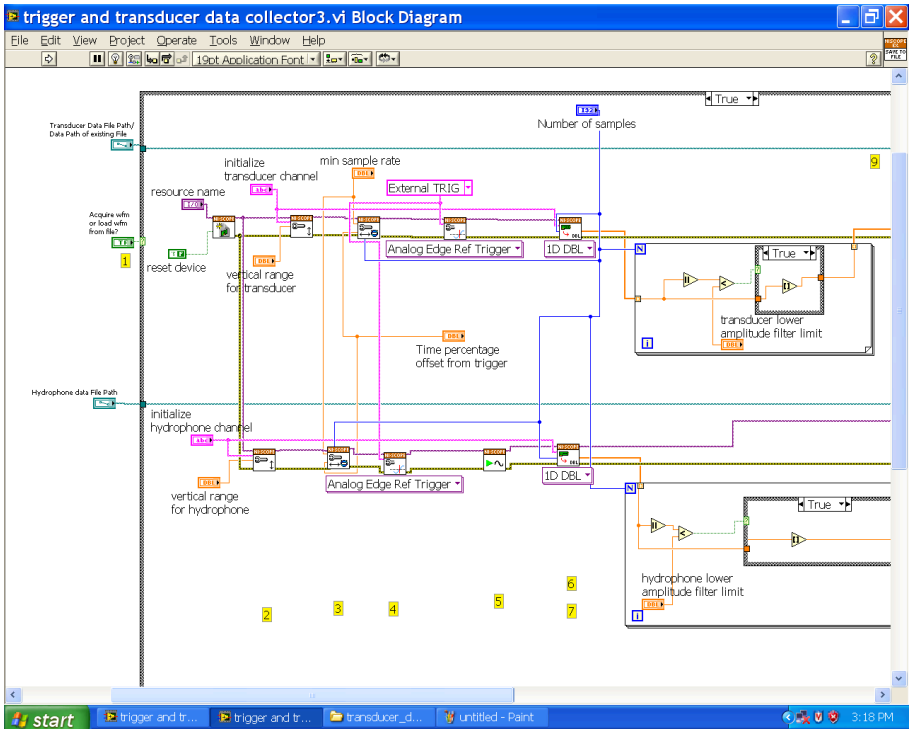

Figure A.1: Left side of block diagram in Labview file that acquires data from PCI-5114 card

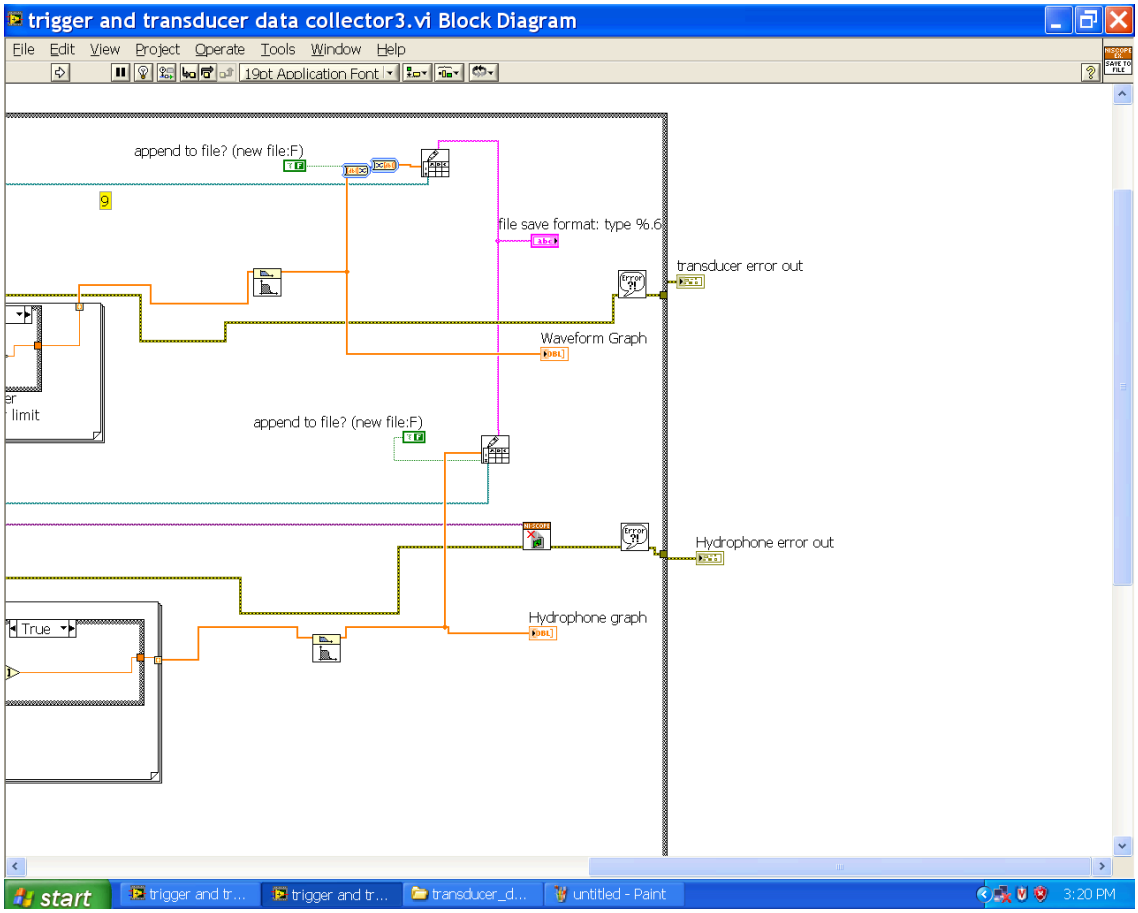

Figure A.2: Right side of block diagram in Labview file that acquires data from PCI-5114 card

The overall organization created for the block diagram is a true/false switch that determines if the user is interested in either taking data from the card, or plotting stored data from an existing file. If the data is to be taken, the green boxes on the far left of the true/false switch box provide a box in the front panel to input the location that the file should be stored.

If the switch is set to acquire data, the resource name asks for the name of the acquisition card that will be used to acquire data. The "NI SCOPE" icon is an express vi (vi is the file extension name for a labview program file) that resets the device, route the resource name and report any error messages to the next vi. From here, the description will follow the top row (transducer configuration). The vertical range vi inputs the information found previously and additionally, asks for which channel to initialize as well as the vertical range the user expects the data to come in at. This allows the card to divide its "y-axis" into invisible increments that optimize the accuracy of each data point collected. This data is transfered through the vi and passed onto the next.

The next vi performs a similar invisible division of the "x axis" which represents time. This vi asks for the minimum sample rate that will be needed to take accurate data. The larger the time interval, the less accurate the amplitude for the peaks and valleys are. The best reference trigger for acquiring voltage information is Analog Edge Reference Trigger." The external trigger setting tells the program that it is not responsible for synchronizing or triggering the the actual signal that it is recording.

The next vi determines the type of information that will be stored and how it will be stored. The options are binary, string, or 2D string. The choice here of a 1D string of numbers (1D double) means that just the voltage will be recorded and it will record the value as a set of numbers. The user input that is important for this vi is the number of samples that will be taken. This determine how many oscillations to record and will determine the size of the text file that will be created.

The number of samples (number of iterations) and the values recorded are then sent to a while loop which filters out the noise created in the acquisition process. The data is sent to a true/false loop who's conditional statement is set by the green question mark in

the corner. The conditional statement is that if the absolute value of the data sample is less than the "transducer lower amplitude filter limit" then the true/false box reads true and the number is rounded down to the nearest integer (always zero in this case). If the box reads false, then the data goes straight through to the next vi. The data is then run through a frequency filter that filters out data with a frequency above 500kHz. This also reduces the noise in the data.

The filtered data is saved to the file specified at the beginning of the program. The purple input is a user interface box that specifies the format that each file is saved in. The title given to this box tells users to type %.6 because 6 digits past the decimal place is a suggested necessary accuracy based on observation. Finally, any error that occurred in the course of the program being implemented is displayed in an error box on the front panel.

The same set of vi's are run through the hydrophone channel (channel 0).

Appendix B

PUMP USER INTERFACE AND ELECTRICAL CONFIGURATION

The pump's electrical/power configuration was all designed and implemented by people who are no longer present in this lab. The information given here is an effort to be inclusive, however, it is likely that no one will be able to recreate the control boxes from the description below.

B.1 User Interface

The pump is manually run using the "Measurement and Automation" program that comes with the card. After initializing the card before each use, the 1D interactive simulation is run. The default settings should not be changed except for the acceleration (4000 steps/sec is the lowest it will go) and the velocity (about 5000 steps/sec is enough for the open tank flow and 1000 steps/sec is enough for the unidirectional flow parts of the experiment). The zero may be set wherever the user wants because the sensors at both ends of the pump will not let it crash into the end.

B.2 Electrical Configuration

The NI Instruments card that is installed in the computer is connected to a converter box that transmits the information from the user interface/NI card to the protoboard. Figure **??** shows images of both the converter box and the protoboard used in this process.

The protoboard is then connected to the stepper motor control device (RMS Technologies -R701 Step Drive). This connects the leads of the stepper motor to the appropriate controls (A, A-, B, B-, ground, etc). The stepper motor itself is from Anaheim Automation (34Y207S-LW8) and is rated for up to 1200 oz-in torque with no load. Figure **??** show these two components.

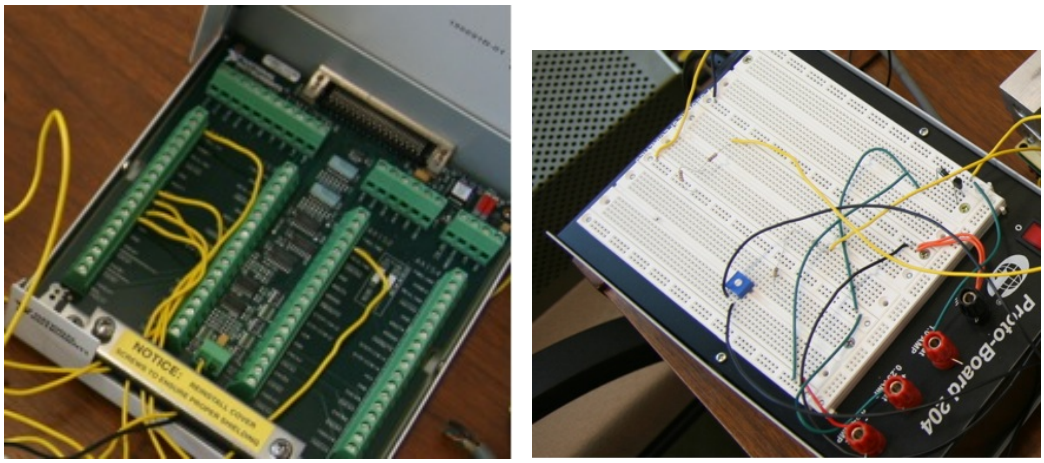

(a) Converter box (b) Protoboard

Figure B.1: The converter box and protoboard used to take command from user interface through the NI card, and onto the motor control device

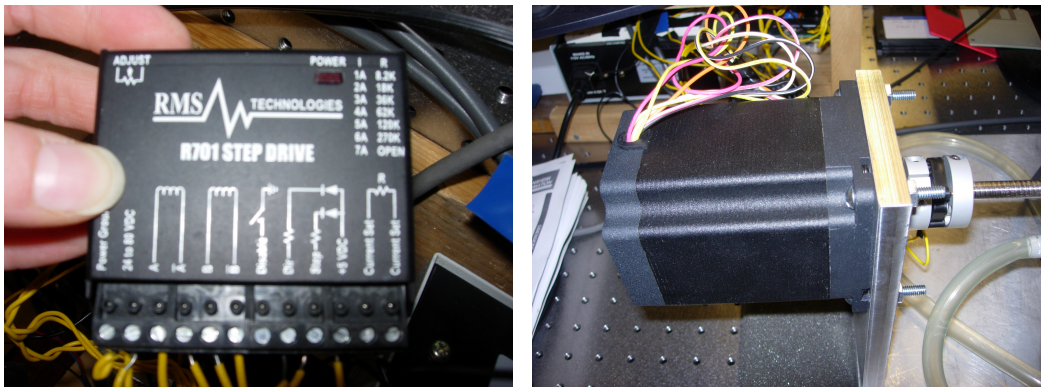

(a) Motor Control Device (b) Stepper motor

Figure B.2: Motor Control Device and Stepper Motor

The motor connects to the end of the threaded shaft with a coupler that grabs onto the key of the motor so it cannot slip. The coupler may be seen on the right hand side of figure **??**.

Appendix C

COMPUTATIONAL FILES USED TO ANALYZE DATA

C.1 0.1 MHz Transducer Pressure Field

This appendix is a verbatim copy of the matlab code used to generate the graph which displays the pressure field as a function of r and z.

```
clear all; close all;



for h=1:28
    j=h*005;

    for k=1:10
       l=k*005-005;
       x(k)=l*10^-1;

 if j<=9 && l<=9
        namefile= sprintf('00%i/00%i.txt',j,l);
elseif j<=99 && l<=9
        namefile= sprintf('0%i/00%i.txt',j,l);
elseif j<=9 && l<=99
        namefile= sprintf('00%i/0%i.txt',j,l);
elseif j<=99 && l<=99
        namefile= sprintf('0%i/0%i.txt',j,l);
elseif j<=999 && l<=9
        namefile= sprintf('%i/00%i.txt',j,l);
```

```
elseif j<=999 && l<=99
        namefile= sprintf('%i/0%i.txt',j,l);

end


      what=fopen(namefile);
      [data,count]=fscanf(what,'%f',300000);
      fclose(what);


       tempmatrix=zeros(10000,30);
       tempmaxvector=zeros(30,1);
       tempminvector=zeros(30,1);

      for m=1:30

          for g=1:10000
              if (((m-1)*10000)+g)<=m*10000
              tempmatrix(g,m)=data((m-1)*10000+g);
              end
          end
          tempmaxvector(m,1)=max(tempmatrix(:,m));
          tempminvector(m,1)=min(tempmatrix(:,m));

      end

    solutionmaxmatrix(h,k)=mean(tempmaxvector);
   solutionminmatrix(h,k)=mean(tempminvector);
```

```
    end

    solutionmaxmatrix2(h,:)=solutionmaxmatrix(h,:);%+(-1/2)*h;


end

col=['r','r','r','r','r','r','b','b','b','b','b','b','g','g'...
,'g','g','g','g','c','c','c','c','c','m','m','m','m','m',];
                                        %solutionmaxmatrix3=solutionmaxmatrix2.';
%for jplot=1:28
    %plot(x,solutionmaxmatrix2(jplot,:),col(jplot)), hold on
    %plot(x,solutionminmatrix(jplot,:),col(jplot)), hold on
%end

for i=1:5
  plot(x,solutionmaxmatrix2(i,:),'r'), hold on
   plot(x,solutionmaxmatrix2(i+5,:),'b'), hold on
    plot(x,solutionmaxmatrix2(i+10,:),'g'), hold on
     plot(x,solutionmaxmatrix2(i+15,:),'c'), hold on
      plot(x,solutionmaxmatrix2(i+20,:),'m'), hold on
end
       %plot(x,solutionmaxmatrix2(26,:),'k'), hold on

title('0.1 MHz Transducer Pressure Field',...
  'FontWeight','bold', 'Fontsize',[20])
xlabel('Radial distance from center of transducer (Inches)','Fontsize',[20])
ylabel('Amplitude of signal (Volts)','Fontsize',[20])
```

```
h = legend('0.5<Z<3','3.5<Z<6','6.5<Z<9','9.5<Z<11.5','12<Z<14',5);
```

C.2 Theoretical Bubble Rise Velocity with/without Transducer

C.3 Experimental Bubble Rise Velocity

C.3.1 Image Processing

This section uses a macro created for the Image J software that subtracts each bubble image from a background image and based on a given threshold, calculates the bubble area, x position, y position and perimeter of the bubble. The scale, threshold and number of pictures are set manually by the user for each set of pictures. The location of the pictures and where the text files should be saved also is updated manually for each set of pictures. The built-in ImageJ functions used include "Analyze Particles", "getImageID", "Measure", "Clear Results" and "Image Calculator." The file is used once for each picture and creates a text file for each picture.

```
macro 'Bubble_info'
{
var num, q, i, j, n, ns, x, ni, pid1, pid2, left, top, width, height, calibmilli, calibpixel,
var  count,loop,renum,dum,a,b,c,d,file,name;//:string;
// begin
// threshold=132;
//{
//setimport('tif');
//}
open("./112008/20_11/background.tif");
pid1 = getImageID();

//PidNumber;
```

```
for (j=1; j<729; j ++)
{
num=j+120;
  if (num<=9){ file="./112008/20_11/img0000"+num+".tif";}

 else if(num<=99) {file="./112008/20_11/img000"+num+".tif";

}
 else if(num<=999) {file="./112008/20_11/img00"+num+".tif";

}
 else {file="./112008/20_11/img0"+num+".tif";

}
  run("Measure");
  run("Clear Results");
  open(file);
  dum = getImageID();

  imageCalculator("sub create 32-bit",pid1, dum);


   run ("Set Measurements..." , "center area perimeter");


   setThreshold(8618,20240,"black & white");

   run ("Analyze Particles...", "minimum=1 maximum=100000 Show=outlines include display'
```

```
   if (j<=9){name="/Users/Cher/Documents/Results/112008/20_11/000"+j+".txt";}

 else if (j<=99) {name="/Users/Cher/Documents/Results/112008/20_11/00"+j+".txt";}

 else if(j<=999) {name="/Users/Cher/Documents/Results/112008/20_11/0"+j+".txt";}

 else {name="/Users/Cher/Documents/Results/112008/20_11/"+j+".txt";}

  //selectWindow('Results');

  saveAs("measurements", name);

  run("Clear Results");
if (nImages>3) {
  close();
}
 close();
 close();
}
```

C.3.2 Data Processing

The following matlab file is placed into each file folder which contains all the text files for a given image sequence. This file opens each of the text files, reads and stores the data and calculates the total, x, and y velocities for a given time interval between each of the pictures. The average over all of the pictures are also calculated and the data is stored in an excel file.

```
%%%%%%%  Rising bubbles  %%%%%%%%%%%
clear all;
del=1;
cont=0;
lold=0;
nimage=32;
fps=500;  %high speed camera set up
inct=1/500;
for last=1:nimage
    if last<=9
        risingbub_file=sprintf('000%i.txt',last);
    elseif last<=99
        risingbub_file=sprintf('00%i.txt',last);
    else
        risingbub_file=sprintf('0%i.txt',last);
    end

    fid=fopen(risingbub_file);
    tline=fgetl(fid);
    [data,count]=fscanf(fid,'%f %f %f %f %f',[5 inf]);
    fclose(fid);
[c d]=size(data);
        if count~=0
            %if data(2,1)>0.5
            time(lold+1:lold+2)=inct*last;
            Area(lold+1:lold+2)=data(2,1);
            x(lold+1:lold+2)=data(3,1);
            y(lold+1:lold+2)=(data(4,1));
    Perim(lold+1:lold+2)=data(5,1);
```

```
            lold=lold+1;
            %end
        end


end
eps=1e-6;
threshold=1;
minimum_value=0.1;
for i=1:lold-1
    if (Area(i)>minimum_value) %&& (y(i+1) - y(i))<.05
   % index=find(abs(time(i+1) - time(i)-inct)<eps)
   % goodbubble=find(Area(index)> minimum_value);
   if (((time(i+1) - time(i))-inct)<eps)
         Vx(cont+1)=(x(i+1) - x(i))/inct;
         Vy(cont+1)=-((y(i+1) - y(i))/inct);
         Vt(cont+1)=(sqrt((Vx(cont+1))^2 + (Vy(cont+1))^2));
         Diameter(cont+1)=(sqrt(4*Area(i)/pi) + sqrt(4*Area(i+1)/pi))/2;
%         Ratio(cont+1)=(Circul(i+1) + Circul(i))/2;
         t(cont+1)=time(i);
         cont=cont+1;

   end
    end
end


ave(1,1)=mean(Diameter(:));
ave(1,2)=mean(Vx(:));
```

```
ave(1,3)=mean(Vy(:));
ave(1,4)=mean(Vt(:));



matrix(:,1)=Vx(:);
matrix(:,2)=Vy(:);
matrix(:,3)=Vt(:);

save 3_2.xls ave -ASCII

plot(t,Vy)
```

C.4 Iteration Code for Determining Theoretical Rise Velocity

The following section shows the Matlab code which iterates through the possible rise velocity values for bubbles of different diameters. The code does not take into consideration the Bjerknes force because many of the values needed for an accurate solution are unknown here. The initial guesses made correspond to the experimental data.

```
  close all; clear all; clc
format long e

rho=1000;
g=9.8;
f=100000;
k=(2*pi*f)/(1500);
P=20278.5;
beta=0.1;
mu=0.001002;

%USED FOR D between 1 and 100 microns
```

```
D=0.000001:0.000001:0.0001;
v(:,1)=0.003:.00012:0.01488;

%USED FOR D between 100 microns and 1 mm
%D=0.0001:0.00000909:0.00099991;
%v(:,1)=0.003:.0015:0.1515;

 for i=2:15

  for j=1:100

      r(j)=(D(j))/2;
      Vol(j)=(4/3)*pi*(r(j))^3;
      Re(j,i)=(rho*v(j,i-1)*D(j))/(mu);

      FBO(j,i)=rho*(4/3)*pi*(r(j))^3*g;
      FD(j,i)=6*mu*pi*r(j)*(1+0.197*Re(j,i)^(0.63)+((2.6*10^(-4))*(Re(j,i)^1.38)));

      v(j,i)=(FBO(j,i))/FD(j,i);
      %dv(j)=0.00005;
      if v(j,i)-v(j,i-1)<10^-3
        v(j,i)=v(j,i);

      else
         v(j,i)=v(j,i);

        end
  end
```

```
  %v(j)=v(j)+dv
end
```

Appendix D

MICROBUBBLE RECIPE

The original microbubble recipe was created by Jonathan Lundt in the Bioengineering Department at the University of Washington. The following is a version of the recipe that is exactly what I did and slightly summarizes the process. There are two solutions, A and B, and each of the first two sections will describe how to make them respectively. The third section will describe how to combine the two solutions and actually make microbubbles.

D.1 Solution A

1)Add

- 2.7 mg of 1,2-Dipalmitoyl-*sn*-Glycero-3-Phosphate (Monosodium Salt)
- 18.1 mg of 1,2-Dipalmitoyl-*sn*-Glycero-3-Phosphoethanolamine-N-[Methoxy(Polyethelene-glycol)-5000](Ammonium Salt)(DPPE-PEG 5000)
- 24.1 mg of 1,2-Dipalmitoyl-*rac*-glycero-3-phosphocholine
- 30 mL of distilled water (using 1 mL pipette)

to a 50 mL beaker. The scale should have an accuracy of at least 0.1 mg. Our scale is the Symmetry ^{TM} PA120 scale from Cole Palmer.

2) Place a stir bar in the beaker and place aluminum foil or Parafilm ^{TM} over most of the open end of the beaker. Leave a little gap in the cover so that steam can escape and the pressure does not build up too much.

3) Place about 20 mL of distilled water into a 150 mL beaker and put the 50 mL beaker from step 2 into in.

4) Put the beakers in the center of the hot plate/magnetic stirrer (ours is a a StableTemp from Cole Palmer). Turn the temperature to med-hi (about 350° C) and the magnetic stirer to 1200rpm. Wait about 10 minutes and check if all the powders are dissolved.

5) After all ingredients are thoroughly mixed, let solution cool before touching either of the beakers and before refrigerating it for future use.

D.2 Solution B

1) Add

- 234 mg of Sodium Phosphate Monobasic, 1-hydrate
- 216 mg of Sodium Phosphate Dibasic, 7-hydrate
- 487 mg of NaCl (table salt)
- 10.00 mL of Glycerin (Glycerol)
- 10.00 mL of Propylene Glycol
- 30.00 mL of distilled water

into a 250 mL screw cap flask.

2) Shake the flask vigorously for at least 2 minutes or until all ingredients have completely dissolved.

D.3 Complete UCA Solution

1) Combine 0.25 mL of Solution A and 0.25 mL of Solution B into a 1.5 mL screw cap septum vial.

2) Place septum vial in amalgamator (YDM Amalgamator from Hang Zhou YinYa New Materials Co. Ltd.) and shake on low for 60-90 seconds.

3) If you are injecting the bubbles directly into the tank, do not dilute them. Otherwise, fill the rest of the vial with distilled or filtered water and use bubbles immediately.